Numerical simulations of granular column collapse

Hugo A. Martin, Marc Peruzzetto, Sylvain Viroulet, Anne Mangeney, Pierre-Yves Lagrée, Stéphane Popinet, Bertrand Maury, Aline Lefebvre-Lepot, Yvon Maday, François Bouchut

Numerical Simulations of Granular Column Collapse: Comparison Between DEM, Navier-Stokes and thin-layer Models

Hugo A. Martin,[1,2,*] Marc Peruzzetto,[3,1] Sylvain Viroulet,[4] Anne Mangeney,[1,5] Pierre-Yves Lagrée,[6] Stéphane Popinet,[6] Bertrand Maury,[7,8] Aline Lefebvre-Lepot,[9] Yvon Maday,[2,5] and François Bouchut[10]

[1] *Institut de physique du globe de Paris, CNRS, Université Paris Cité, F-75005 Paris, France*
[2] *Laboratoire Jacques-Louis Lions, (LJLL), CNRS, Sorbonne Université, Université de Paris, F-75005 Paris, France*
[3] *BRGM, F-45060 Orléans, France*
[4] *Institut de Mécanique des Fluides de Toulouse (IMFT), Université de Toulouse, CNRS-INPT-UPS, Toulouse, France.*
[5] *Institut Universitaire de France*
[6] *Institut Jean le Rond ∂'Alembert, Sorbonne Université, CNRS UMR 7190, F-75005 Paris, France*
[7] *Département de Mathématiques Appliquées, École Normale Supérieure, Université PSL, Paris, France*
[8] *Laboratoire de Mathématiques d'Orsay, Université Paris-Saclay, 91405 Orsay Cedex, France*
[9] *CMAP, CNRS, École Polytechnique, Institut Polytechnique de Paris, 91128 Palaiseau Cedex*
[10] *Laboratoire d'Analyse Mathématiques Appliquées, CNRS UMR 8050, Université Gustave Eiffel, UPEC, Marne-la-Vallée F-77454, France*

(Dated: October 27, 2022)

Abstract: Granular flows occur in various contexts including laboratory experiments, industrial processes and natural geophysical flows. In order to investigate their dynamics, different kinds of physically-based models have been developed. These models can be characterized by the length scale at which dynamic processes are described. Discrete models use a microscopic scale to model individually each grain, Navier-Stokes models use a mesoscopic scale to consider elementary volumes of grains, and thin-layer models use a macroscopic scale to model the dynamics of elementary columns of fluids. In each case, the derivation of the associated equations is well known. However, few studies focus on the extent to which these modeling solutions yield mutually coherent results. In this work, we compare the simulations of a granular column collapse on a horizontal or inclined plane, for the discrete model COCD, the Navier-Stokes model Basilisk, and the thin-layer model SHALTOP. We show that, although all three models allow reproducing the temporal evolution of the free surface in the horizontal case (except for SHALTOP at the initiation), the modeled flow dynamics are significantly different, and in particular during the stopping phase. The pressures measured at the flow's bottom are in relatively good agreement, but significant variations are obtained with the COCD model due to complex and fast-varying granular lattices. Similar conclusions are drawn using the same rheological parameters to model a column collapse on an inclined plane. This comparison exercise is essential for assessing the limits and uncertainties of granular flow modeling.

Keywords: Granular Media, Discrete Element Methods, Navier–Stokes Equations, Thin-layer Models, Granular Flow Dynamics, Basal Stress

INTRODUCTION

Dry granular flows have been widely studied over the past decades, from industrial processes [1, 2] to geophysical flows such as rockfalls [3–5], rock and debris avalanches [6–8], pyroclastic flows [9, 10], or more generally, dry landslides both on Earth and other planets [11, 12].

Laboratory experiments allow investigating the physical processes controlling granular flow dynamics, such as self-channeling [13–15], particle size segregation [2], and bed erosion [16–18]. Nevertheless, some key flow characteristics are challenging to measure in experiments but can be directly estimated in numerical simulations, like the pressure inside the flow or the velocity field. Numerical modeling also helps to validate physically-based models used to describe the processes at stake [4, 19–21], to investigate configurations difficult to set up in a laboratory, and flows at a larger scale such as at the field scale for geophysical flows.

Multiple modeling solutions exist depending on the scale of the flow description, rheological laws, and numerical methods. At the microscopic scale, simulations with discrete models, generally referred to as Discrete Element Methods (DEM), represent the granular flow by many distinct particles, and all grain-to-grain interactions are modeled [22–25]. This approach is supposedly the most realistic but has a high computational cost as the number of particles increases [e.g., 26–28]. It limits their applicability to flows at larger scales. Furthermore, the large range of particle sizes that change in time due to fragmentation is still poorly handled despite the strong effect of particle segregation in granular flows [29]. A second modeling solution considers the granular flow as a continuous medium and solves the Navier-Stokes equations to model the dynamics of each elementary volume [e.g., 30–33]. In this case, larger events can be modeled but the main difficulty remains in the definition of suitable rheological laws. Furthermore, simulating natural flows over complex topography still

* martin_hugo@ymail.com

requires huge computational cost, which complexifies sensitivity analyses [34]. A third modeling option is based on the thin-layer approximation where the flow's thickness is assumed to be small compared to its extent, and velocity is assumed to be parallel to the slope. Consequently, the model only solves for the thickness of the flow and its depth-averaged velocity. These models are often used empirically because the rheological parameters are calibrated to reproduce experiments or field observations [12]. However, thanks to their relatively low computational cost, they can be used at field scale to reproduce real geophysical events. Since the pioneering work of [35–37], they have been widely used for physics-based landslide hazard assessment [38–40]. Note that unlike the first option using discrete models, the Navier-Stokes and thin-film models cannot represent blocking effects between particles due to the continuous formulation of these models.

All these models are classically tested by comparing observed and simulated landslide travel distance (or runout) and deposits extent and thickness. Indeed, these characteristics are the easiest to observe on the field for geophysical flows. However, over the past decades, seismic waves generated by these flows have been increasingly used to constrain their dynamics (both at the laboratory and at the field scales *e.g.* [41–44]). In turn, seismic waves can be used to calibrate both thin-layer models [45–48] and discrete models [49, 50]. This is done, in particular, by comparing the basal force inverted from seismic signals and deduced from simulations (*e.g.*, [48, 50]). Thus, to accurately interpret the comparison between simulations and observations and be aware of their limitations, it is essential to understand how the dynamics (and in particular the basal force) of the simulated flow depends on the type of simulation tool. To the best of the authors' knowledge, no systematic comparison between discrete, Navier-Stokes, thin-layer models, simultaneously with experimental data, has been performed so far.

In this work, we investigate the discrepancies between discrete, Navier-Stokes and thin-layer models, with three numerical codes: the discrete model Convex Optimization Contact Dynamics (COCD) [51], the Navier-Stokes model Basilisk [52], and the thin-layer model SHALTOP [20, 53–56]. In order to allow for a more straightforward interpretation, we consider the simple case of a column collapse, reproducing the experiments of [17] for three slope angles $\theta = 0°, 10°$ and $16°$. Rheological parameters are chosen to match the profiles of one column collapse experiment. We compare these methods on their profiles evolution, deposits, dynamics, and normal stresses on the ground. In Section I, we present the experimental data used to calibrate the model. Then, in Section II, we describe the three different numerical models. Simulations results are presented in Section III, then simulations of flow dynamics and basal normal stresses are discussed in Section IV. An additional spectral analysis of COCD normal stress is done in the same section, with a discussion on rheological parameters, see Section IV.

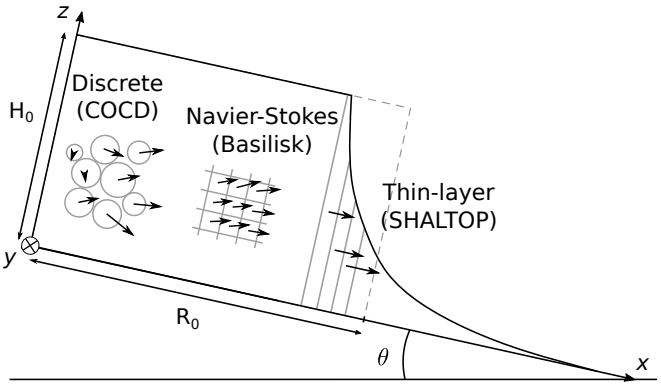

FIG. 1. Three different types of models to simulate granular column collapse. Black arrows represent velocity vectors. In the discrete model (COCD) every disc has its own velocity, in the Navier-Stokes model (Basilisk) the velocity is defined in each cell while in the thin-layer model (SHALTOP), a depth-averaged velocity, parallel to the bed, is associated to each column. The dashed gray line represents the contour of the initial rectangular mass released from rest at $t = 0$ s.

I. EXPERIMENTAL SETUP

The experimental setup used in the simulations is described in detail in [17]. It consists of a 3 m long channel of width 20 cm and inclination θ between 0° and 30°. Let us define a cartesian reference frame (x, y, z) linked to the bed, such that the z-axis is perpendicular to the bed and the x-axis is pointing in the downslope direction. In this reference frame, the channel base is given by $z = 0$ (see Fig. 1).

The granular material consists of spherical glass beads released from rest as a rectangular mass of height $H_0 = 14$ cm and length $R_0 = 20$ cm. The corresponding aspect ratio is $a = H_0/R_0 = 0.7$. The mean diameter of beads is $d = 0.7 \pm 0.1$ mm. A layer of glass beads is glued to the plane. The initial mass is released by opening a gate in the direction perpendicular to the channel bed.

The experimental setups reproduced in our simulations correspond to slope angles $\theta = 0°$ and $\theta = 16°$. $\theta = 10°$ and $\theta = 22°$ are also considered for comparison. The manner in which the initial state is constructed in simulations is described in detail in Appendix A.

II. NUMERICAL MODELS

The general concepts and equations of the different models used in this work are now briefly presented. More details on the simulation setups and output processing are given in Appendix A and B. The values of numerical parameters are given in Table I, Appendix C. The flow

dynamics is solved on a 2D domain only. Interactions between the beads and lateral walls are thus not taken into account explicitly. The initial granular column is released from rest without accounting for the gate's initial lifting (see [31] for the effects of the gate).

A. The discrete model COCD

In discrete models, the granular mass is represented by a collection of rigid particles (see Fig. 1) like glass discs (or spheres in 3D). The motion equations are solved at each time step for all of these particles, determining their contact forces. Their interactions can be classically modeled through the Hertz theory, using non-linear damp springs, as done in the Molecular Dynamics (MD) approach (see the seminal work of Cundall [22]). In this work, we use another approach named Contact Dynamics (CD), firstly introduced by Moreau and Jean in the 1990s [23, 57–61]. Unlike MD, where the contact forces are modeled by functions obtained from Hertz theory, in CD, the forces are linear impulses, submitted to contact laws describing normal repulsion and tangential friction that are included into the Newton's second law of motion.

Numerous numerical methods have been proposed for CD models [24, 51, 62–67]. Classically, one shall specify the normal and tangential contact laws, which must be verified for every contact and time step. The normal law is based on a non-overlapping constraint, a complementary relation between the normal distance and the intensity of the normal contact force. It means that grains cannot overlap or interact if they are not in contact, and the force between two grains is always repulsive, *i.e.,*

$$0 \leq \mathrm{D}^\alpha, \qquad \mathrm{f}_\mathrm{n}^\alpha \mathrm{D}^\alpha = 0, \qquad \mathrm{f}_\mathrm{n}^\alpha \geq 0, \tag{1}$$

where α is the number associated to a contact between two particles, D^α is the normal distance that measures the gap between the two particles, and f_n^α is the normal force intensity between them. These relations are supplemented by the inelastic contact law. The tangential contact law that is verified for all contacts is the Coulomb friction law, involving the tangential and normal components of the contact force belonging to Coulomb's cone, *i.e.,*

$$\begin{array}{rcll} \mathrm{f}_\mathrm{t}^\alpha & = & -\mu_p \mathrm{f}_\mathrm{n}^\alpha \, \mathrm{v}_\mathrm{t}^\alpha / \|\mathrm{v}_\mathrm{t}^\alpha\|, & \text{if } \|\mathrm{v}_\mathrm{t}^\alpha\| > 0, \\ \|\mathrm{f}_\mathrm{t}^\alpha\| & \leq & \mu_p \mathrm{f}_\mathrm{n}^\alpha, & \text{if } \|\mathrm{v}_\mathrm{t}^\alpha\| = 0, \end{array} \tag{2}$$

where μ_p is the friction coefficient between the particles, $\mathrm{f}_\mathrm{t}^\alpha$ is the tangential force vector, and $\mathrm{v}_\mathrm{t}^\alpha$ is the tangential relative velocity vector between the two particles involved in the contact α.

In this paper, to compute the approximated solution of the motion equation including the contact laws (1) and (2), we use the numerical method called Convex Optimization Contact Dynamics (COCD), described in [51]. In this particular approach, the numerical scheme is a natural discretization of Newton's second law and the non-overlapping constraint (1) is convexified. Doing so, the grains velocities and positions may be computed simultaneously using an implicit scheme, which requires solving a convex minimization problem with conic constraints at each time step.

The mechanical behavior of such discrete media results from a combination of geometrical rearrangements between particles and inter-particle friction forces. In our discrete model, the only rheological parameter is the inter-particle friction coefficient mu_p, present in the tangential law (2), and which is calibrated to reproduce laboratory experiments. More precisely, the macroscopic static friction coefficient $\mu_s = \tan(\theta_m)$ – where θ_m is the static friction angle, *i.e.,* the angle that the granular mass forms at rest – can be interpreted as the combination of the inter-particle friction coefficient μ_p and the geometric trapping (dilatancy effect) μ_g [68]. The coefficient μ_g is linked to the grains' shapes, masses, or inertia, while μ_p is a given parameter of the model, and used in the classical Coulomb's law of friction at any grain/grain or grain/wall contact [51].

In this paper, 2D simulations only are considered for comparing the three models. The value for μ_p used here is derived from back-analysis by reproducing the deposits from experiments through 2D simulations in the horizontal case. The best-fit interparticle friction coefficient is $\mu_p = 0.9$. Note that this value is relatively large compared to the friction coefficient $\mu_p = 0.3$, calibrated by comparing 3D simulations and experiments [51], and which is in the range of friction coefficients measured for a perfect glass/glass contact $\mu = 0.4$ [69], and that measured with MD $\mu = 0.16$ [70]. In COCD, this difference in calibrated friction coefficients arises when comparing mass profiles in 2D and 3D simulations. We discuss this point in Section IV E.

B. Basilisk

Basilisk [52] is a continuum multiphase flow solver based on a finite volume method (see Fig. 1) and Volume-Of-Fluid approach to track the interface between phases. In our case, these two phases are air and granular phase. The eulerian mesh grid remains constant in the granular material and coarsens in the air (see figure 2 of [71] for an illustration). Basilisk solves the local incompressible mass and momentum equations :

$$\nabla \cdot \mathbf{V} = 0, \tag{3}$$

$$\rho \left(\frac{\partial \mathbf{V}}{\partial t} + \mathbf{V} \cdot \nabla \mathbf{V} \right) = \rho \mathbf{g} - \nabla p + \nabla \cdot (2\eta D), \tag{4}$$

where $\mathbf{V} = (V_x(x,z,t), V_z(x,z,t))$ is the velocity field with components V_x and V_z in the x- and z-direction, respectively, $\mathbf{g}$ is the gravity field, ρ is the density, and η the dynamic viscosity. This is equivalent to writing the

stress tensor σ as

$$\sigma = -pI_d + \sigma', \tag{5}$$
$$\sigma' = 2\eta D, \tag{6}$$

where σ' is the deviatoric stress tensor, I_d is the identity tensor and the strain rate tensor is

$$D = \frac{1}{2}\left(\nabla \mathbf{V} + \nabla \mathbf{V}^t\right). \tag{7}$$

Basilisk thus solves the velocity field and the pressure in the granular phase provided a constant value or a rheological law is given to define η.

The $\mu(I)$-rheology has met with growing success to model granular flows [72, 73]. When considering simple shear dry granular flows, dimensional arguments and numerical simulations showed that the shear stress is proportional to the pressure p, through a coefficient μ that depends on the inertial number I. The tensor formulation of this rheology is [73]:

$$\sigma' = \frac{\mu(I)p}{\|D\|}D, \tag{8}$$
$$\text{with} \quad I = \frac{2\|D\|d}{\sqrt{p/\rho}}, \tag{9}$$

with $\|D\| = \sqrt{0.5 D_{ij} D_{ij}}$ and d the mean diameter of grains belonging to the granular phase. Thus, the $\mu(I)$-rheology boils down to considering a viscous fluid, with a non-constant viscosity η:

$$\eta = \frac{\mu(I)p}{2\|D\|}. \tag{10}$$

Finding an explicit and general relation between the coefficient μ and the inertial number I is an open question. The most common expression of $\mu(I)$ derived for steady flows on constant slopes is given by:

$$\mu(I) = \mu_1 + \frac{\mu_2 - \mu_1}{1 + I_0/I}, \tag{11}$$

where μ_1, μ_2 and I_0 are constants. But the resulting model may be ill-posed: small-scale instabilities in the flow can significantly affect simulations results [32, 74]. Nevertheless we use this expression. Furthermore, to avoid numerical divergence when $\|D\|$ tends to 0 in Equation (10), a maximum value for the viscosity $\eta_{max} =$ 24000 Pa s is imposed following [30] to regularize the problem when the strain rate tends to zero.

The friction coefficients are $\mu_1 = 0.48$, $\mu_2 = 0.73$ and $I_0 = 0.279$. Solving the same equations, they have been calibrated for $a = 0.7$ and $\theta = 0°$ through an Augmented Lagrangian method and were quantitatively compared to granular collapse experiments [31]. Note that these rheological parameters have been slightly overestimated compared to experimental measurements [73] to take into account the wall effects. For a detailed analysis of wall effects in Navier-Stokes and thin-layer models, see [32] and [75], respectively. A discussion about the influence of the rheological parameters is presented in Section IV.

C. SHALTOP

Depth-averaged thin-layer granular flow simulations are carried out with the SHALTOP numerical code [20, 53–56]. This code has been successfully used to simulate both laboratory experiments [55] and field scale landslides on Earth and other planetary bodies, *e.g.*, [12, 45, 76–78]. SHALTOP also proved to accurately reproduce analytical solutions of the dam-break problem [79–81] and was compared to other depth-averaged models in one of the only benchmark exercise for these types of codes [82].

To match as closely as possible the equations implemented in Basilisk, we use a depth-averaged version of the $\mu(I)$-rheology following [19, 20, 83]. The resulting mass and momentum equations are:

$$\frac{\partial h}{\partial t} + \frac{\partial (h\overline{V})}{\partial x} = 0, \tag{12}$$
$$\frac{\partial (h\overline{V})}{\partial t} + \frac{\partial (h\overline{V}^2)}{\partial x} = S_1, \tag{13}$$

with

$$S_1 = gh\cos(\theta)(\tan(\theta) - \frac{\partial h}{\partial x}) - gh\cos(\theta)\mu(I)\frac{\overline{V}}{|\overline{V}|}. \tag{14}$$

The term S_1 includes the gravitational and longitudinal pressure forces, and a bottom friction force where $\mu(I)$ appears. As for Basilisk, $\mu(I)$ is given by Equation (11), but with the depth-integrated version of the inertial number I:

$$I = \frac{5du}{2h\sqrt{gh\Phi\cos(\theta)}}, \tag{15}$$

where Φ is the volumetric solid fraction.

Note that in the derivation of the corresponding thin-layer equations for flows on inclined planes given in [83, 84], an additional viscous term S_2 appears on the right-hand side of Equation (13):

$$S_2 = \frac{\partial}{\partial x}\left(\nu h^{3/2}\frac{\partial \overline{V}}{\partial x}\right), \tag{16}$$

where ν is a coefficient that can be related to bed slope, μ_1 and μ_2 [see Equations 4.16 in 84]. However, the expression of ν in [84] is valid for steady flows only, when $\mu_1 < \tan(\theta) < \mu_2$, which is not the case in our simulations. More generally, it is not valid for complex, non planar topogaphies. As we want our results to help improve the interpretation of thin-layer simulations at the field scale, we will thus not consider the viscous term S_2 in our simulations. Besides, comparisons with experiments in Section III A show that the depth-averaged $\mu(I)$-rheology without viscosity already allows to match correctly granular collapse deposits.

We use the same rheological parameters as for Basilisk simulations: $\mu_1 = 0.48$, $\mu_2 = 0.73$ and $I_0 = 0.279$.

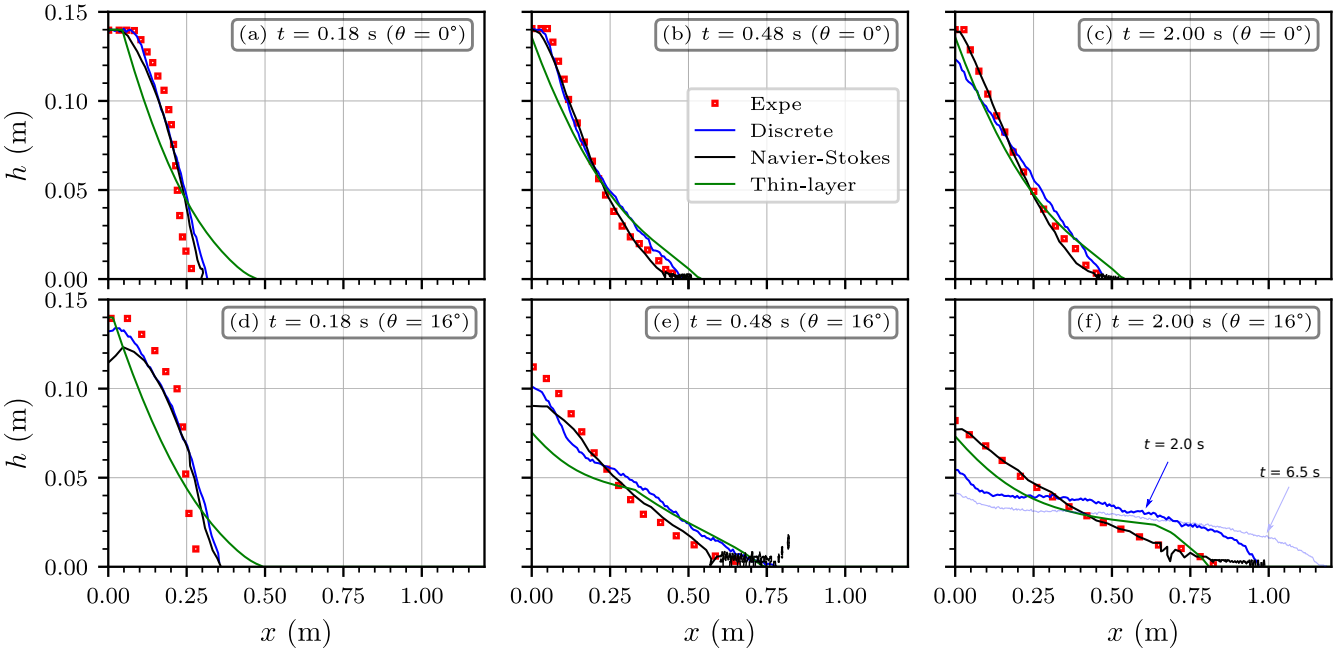

FIG. 2. Comparison between experiments and numerical simulations of the granular profiles during a column collapse. We display the experiment results (red squares), discrete COCD simulations (blue line), Navier-Stokes Basilisk simulations (black line) and thin-layer SHALTOP simulations (green line). The initial aspect ratio is $a = 0.7$, with a bed slope $\theta = 0°$ (a, b, c) and $\theta = 16°$ (d, e, f). The light blue line in (f) is the discrete simulation profile at $t = 6.5$ s.

For simplicity, the solid fraction in Equation (15) is set to $\Phi = 1$, as it allows to match mass profiles observed in experiments and simulated with Basilisk, both for $\theta = 0°$ and $\theta = 16°$. We tested $\Phi = 0.6$, and results are very similar to $\Phi = 1$. Thus, in thin-layer simulations, the main controlling parameters are the friction coefficients μ_1 and μ_2, and not the volume fraction Φ. We investigated the sensitivity of the results to μ_1 and μ_2 in Section IV D.

III. RESULTS

To compare the discrete, Navier-Stokes and thin-layer models together, and with laboratory experiments, we focus on the spatio-temporal change of the flow thickness $h(x,t)$, the position of the flow front $x_f(t)$, the velocity field and the arrest phase, as well as on the basal normal stress σ_b and the hydrostatic pressure p_h, both applied by the flow to the bed. Appendix B details how all these quantities are computed in the different models, and Table I in Appendix C gives all numerical parameters.

A. Granular mass profiles

1. *Horizontal plane*

The first row of Fig. 2 shows comparisons between experimental measurements of the granular mass profile on a horizontal plane ($\theta = 0°$) and the different numerical models at three different times. After the column release at $t = 0$ s, the mass spreads on the plane, decelerates, and stops to form a deposit. The mass profiles obtained with the Navier-Stokes model Basilisk reproduce very well the overall granular spreading (compare black line and red squares in Fig. 2). Moreover, the final deposit is in excellent agreement with the experiment, although the initial spreading is slightly faster in the simulation (Fig. 2a).

The profiles resulting from the discrete model are initially very similar to those obtained using the Navier-Stokes model. However, the final deposit slightly differs from the experiment, with a concave shape of the frontal part while the deposit front is slightly convex (Fig. 2c and f).

The depth-averaged thin-layer model SHALTOP overestimates the initial spreading. However, despite the initial overestimation of the velocity, the final deposit is in good agreement with the experiments with a runout distance overestimated by less than 15%.

2. *Inclined plane*

The second row of Fig. 2 shows similar profiles of the granular mass on an inclined plane $\theta = 16°$, simulated with the same rheological parameters as for the horizontal plane. In this case, the results are more sensitive to the numerical model used. The

thin-layer model SHALTOP is faster than the others but yields a final deposit in good agreement with the experiment. The mass profile has a concave and rounded front compared to the thin experimental front, and the thickness at the rear of the flow decreases faster.

The Navier-Stokes model Basilisk is in good agreement with the experiments throughout the collapse although, the flow being faster than on the horizontal case, some drops and bubbles appear at the front as numerical artifacts (see Section IV A). At $t = 1.02\,\mathrm{s}$, a thin layer (lower than 3.5 mm) develops, which is not observed in the experiments. The overall profile is also slightly less convex than in the experiment, and the upper left thickness of the flow is decreasing faster as in the thin-layer model.

The most significant difference with the experiment is observed for the discrete model COCD, where the flow is still moving after 2 s (compare blue and pale blue lines in Fig. 2f, giving the flow thickness at $t = 2.0$ s and $t = 6.5$ s respectively). This difficulty in stopping the granular flow for $\theta = 16°$ is discussed in Section IV.

B. Flow dynamics

We define the flow's front position $x_f(t)$ as the maximal length reached by the flow, thicker than five-grain-diameters height in experiments, i.e., $h(x_f) \geq 5d = 3.5\,\mathrm{mm}$. The front position is represented for each simulation by a green dashed line in Fig. 3. The left position of the mass is always located at $x = 0$, whatever the time. The way the front is computed is explained in Appendix B. The colors in Fig. 3 represent the depth-averaged downslope velocity $\bar{V}_x(x,t)$ and its space-time evolution at $\theta = 0°$ (Fig. 3a-c) and $\theta = 16°$ (Fig. 3d-f). The velocities represented in white are those smaller than the cutoff velocity $1\,\mathrm{cm\ s^{-1}}$, set as in [17]. It highlights the spatio-temporal characteristics of the stopping phase.

To describe the dynamics of the column collapse, we define three different phases. First, the *acceleration phase* starts when the gate is instantaneously removed and ends when the front reaches its maximal velocity. The *deceleration phase* follows, and we arbitrarily define its end when the front stops, even if the rest of the mass may still be flowing. Finally, the *stopping phase* follows and ends when all the material is at rest. The end of the acceleration (resp. deceleration) phase is represented by a vertical white dashed line (resp. dotted black line) in Fig. 3.

The transition between static and moving state within the granular mass are given by black and gray arrows in Fig. 3. The black arrow correspond to a rarefaction wave propagating from the front to the back of the flow, initiating the movement of materials initially at rest. On the contrary, grey arrow correspond to stopping waves, when materials in movement come to rest. This stopping wave can be initiated at the front of the flow towards the back (Fig. 3b), from the back towards the front (Fig. 3d), or from any location within the mass towards the front or the back (Fig. 3c).

1. *Acceleration phase*

Figs. 3a-c at $\theta = 0°$ show a significant difference between the thin-layer and the two other models in the acceleration phase of the granular mass. This phase is very fast, if not instantaneous, in the thin-layer model: less than 0.02 s, when simulations outputs are written every 0.01 s. It is more progressive in the discrete (0.24 s) and Navier-Stokes (0.22 s) models, in better agreement with experiments (black squares). The propagation of the static/flowing interface (transition between violet and white colors along the black arrows in Fig. 3) towards the left of the column in the thin-layer model is also different from the other models (Figs. 3a-c). Indeed, this interface propagates with an almost constant velocity in the thin layer model while, in the discrete and Navier-Stokes models, it propagates with decreasing velocity. In the Navier-Stokes model, the static/flowing interface stays almost at the same position $x = 0.12\,\mathrm{m}$ for $t > 0.1\,\mathrm{s}$ (Figs. 3c).

The lighter colors in Fig. 3a compared to Figs. 3b,c show that the maximum depth-averaged velocity $\bar{V}$ in the thin-layer model is always higher than in the other models (above $1.1\ \mathrm{m\ s^{-1}}$).

For a column collapse on the inclined plane $\theta = 16°$, Figs. 3(d-f) show qualitatively the same behavior during the acceleration phase as on the horizontal plane. Although velocities are higher, acceleration duration are similar to the horizontal slope case (instantaneous for SHALTOP, 0.24 s for COCD and 0.20 s for Basilisk). In comparison, in the experiments, the acceleration phase lasts 0.26 s and 0.29 s for $\theta = 0°$ and $\theta = 16°$ respectively.

2. *Deceleration phase*

On a flat bottom (Figs. 3a-c), the deceleration phases have a similar duration in the discrete COCD and Navier-Stokes Basilisk simulations (about 0.2 s, between white dashed and black dotted lines in Figs. 3b-c). The portion of the initial mass that does not move on the left is slightly larger with the Navier-Stokes model ($x \leq 0.12$ m compared to $x \leq 0.085\,\mathrm{m}$ for the discrete model).

In the thin-layer model SHALTOP the maximum velocities are higher (above $1\ \mathrm{m\ s^{-1}}$, compared to less than $0.7\ \mathrm{m\ s^{-1}}$ in the other models), as expected. As the acceleration phase is instantaneous, the deceleration phase last the whole flow duration and ends at $t = 0.32$ s. It is sooner than the Navier-Stokes and discrete models (0.45 s for both, black dotted lines in Figs. 3a-c). Finally, the motion still propagates backward throughout the deceleration phase in the thin-layer simulations, while the static/flowing transition almost stays at the same position in the discrete model and only

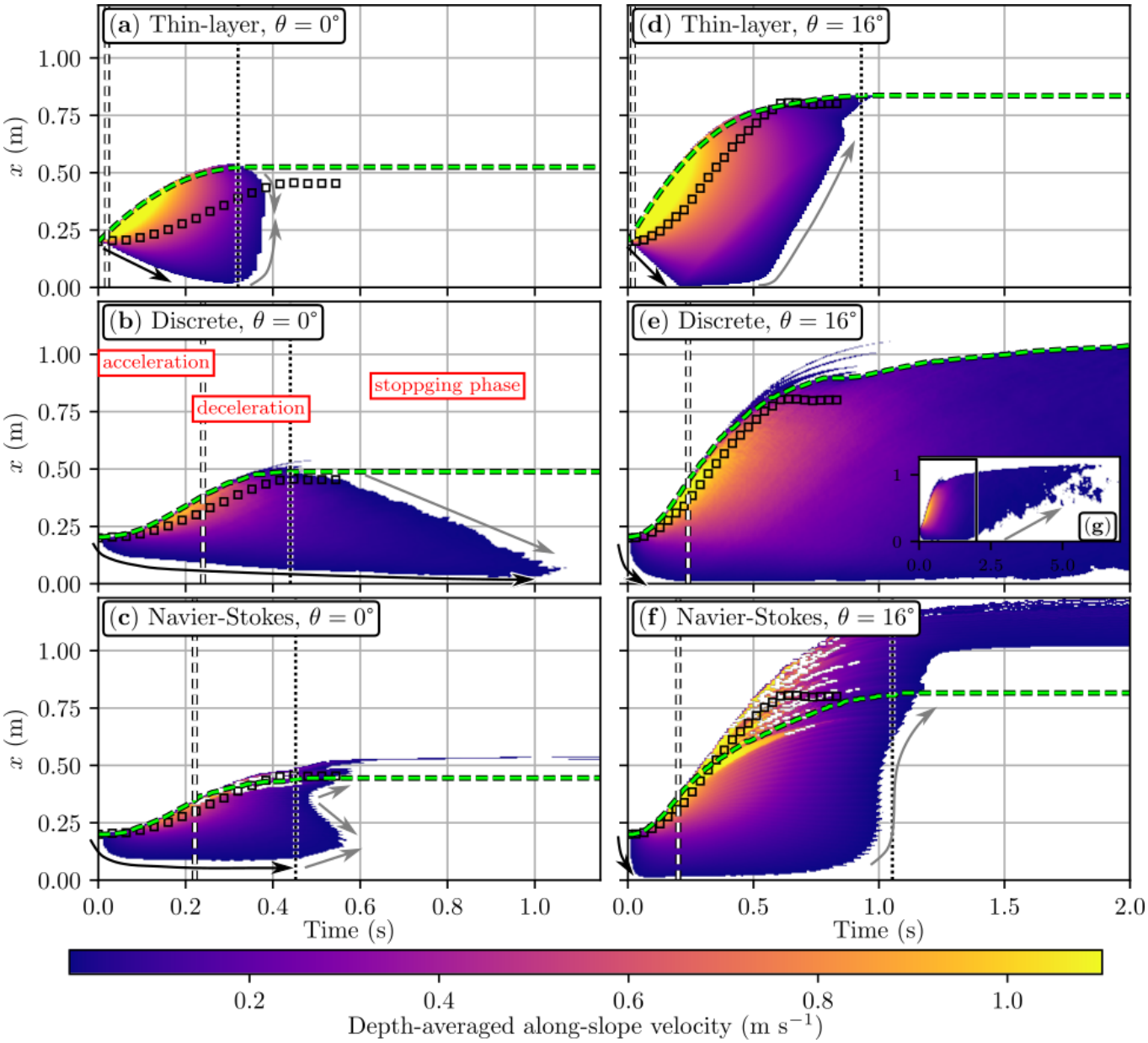

FIG. 3. Spatio-temporal plot representing the depth-averaged along-slope flow velocity $\bar{V}_x(x,t)$ (colorscale) for the different models, with $\theta = 0°$ (a,b,c) and $\theta = 16°$ (d,e,f). We only display velocities above 1 cm s^{-1} (lower velocities are represented in white), as in the experiments of [17]. For each simulation, the green dashed line represents the time evolution of the front position. The acceleration and deceleration phases are separated by a vertical white dashed line, and the deceleration and stopping phases by a vertical black dotted line. Black arrows follow the rarefaction wave where the mass initially at rest is set in motion. Grey arrows follow the stopping wave where the moving mass stops. Black squares give the front position in experiments.

slightly propagates backward in the Navier-Stokes model (compare black arrows in Figs. 3a-c).

In the thin-layer simulation at $\theta = 16°$, the static/flowing transition (rarefaction wave) propagates towards the back during a shorter duration than in the horizontal bed case (compare black arrows of Figs. 3a and 3d), and reaches the rear of the initial mass after about 0.2 s (black arrow in Fig. 3d). Between $t = 0.2$ s and $t = 0.6$ s, almost the whole mass is moving. Then, after $t = 0.6$ s, the stopping wave (gray arrow in Fig. 3d) propagates at constant speed towards the flow's front.

A qualitatively similar but more complex behavior is observed in the Navier-Stokes model at $\theta = 16°$, but at a latter time (from $t \simeq 0.7$ s, Fig. 3f). The flow front is also more contaminated by drops and air bubbles than at $\theta = 0°$ due to increased flow front velocity (compare colors irregularities between Fig. 3c and Fig. 3f). The stopping waves are initiated during the deceleration phase for $\theta =$

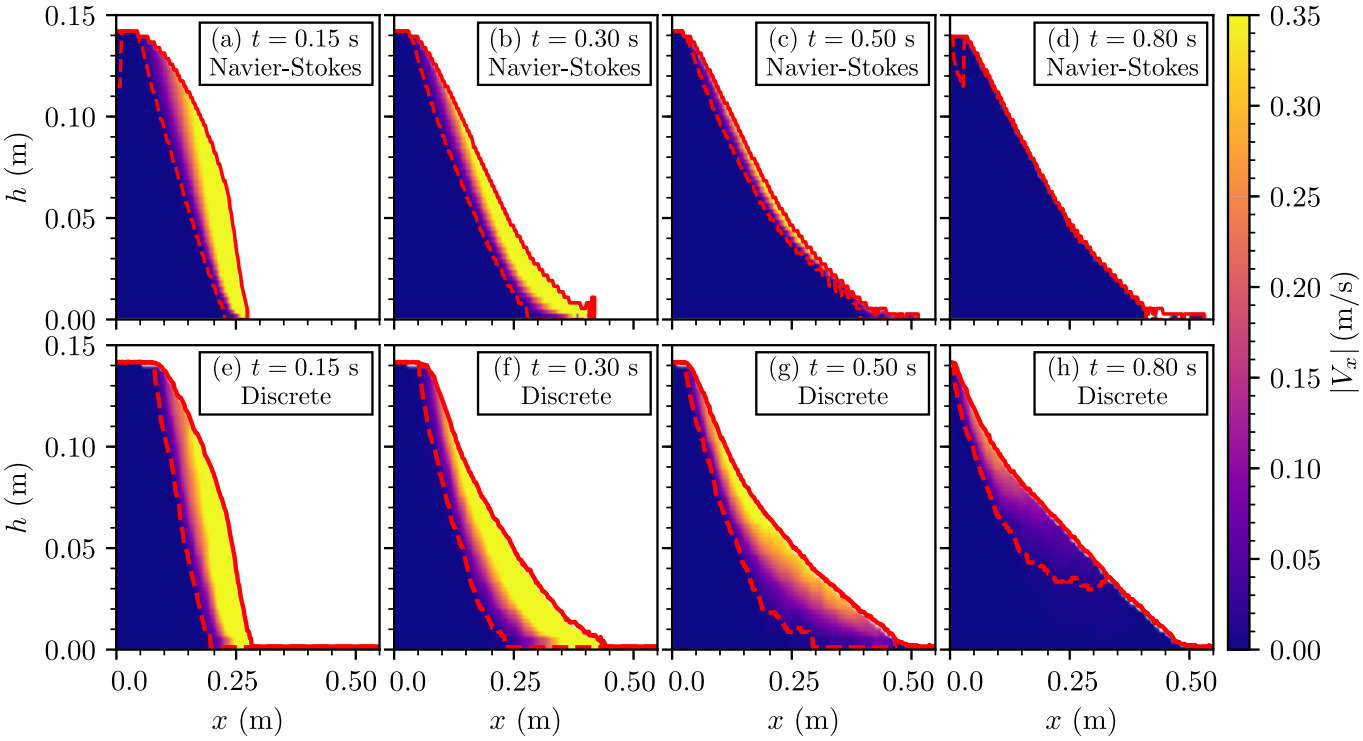

FIG. 4. Comparison between the horizontal velocity V_x calculated with the Navier-Stokes (Basilisk) (first row) and discrete (COCD) (second row) simulations, for $\theta = 0°$. The red continuous line represents the free surface while the red dashed line the static/flowing transition, considering a threshold value $V_x = 1$ cm s^{-1}, as in [17]. Figures (a,e) belong to the acceleration phase, (b,f), to the deceleration phase and (c,d,g,h) to the stopping phase.

16°, from the left wall and propagates faster than in thin-layer and discrete simulations (the flow almost stops at $t = 1$ s).

3. *Stopping phase*

On the horizontal bottom, the stopping phases are very different from one model to the other. The stopping phase simulated by the thin-layer model is very short, less than 0.1 s (Fig. 3a). The granular mass stops from both the front and the rear in an almost symmetrical way (gray arrows in Fig. 3a). The stopping phase simulated with the Navier-Stokes model lasts slightly longer (about 0.15 s) but displays three stopping waves: one from the rear towards the front and two from the middle of the flow propagating in opposite directions (Fig. 3c). This is a direct consequence of the stopping criteria in the Navier-Stokes code Basilisk, see Section IV A. In discrete simulations, the stopping phase is more extended (about 0.6 s), with only one stopping wave propagating from the front to the rear at almost constant velocity (about 0.7 m s^{-1}, Fig. 3b).

On the inclined plane $\theta = 16°$, the stopping phase is different from that observed at $\theta = 0°$. This phase is almost nonexistent in the thin-layer simulations as the front is the last portion of the flow still in motion. Similar qualitative behavior is obtained with the Navier-Stokes model if we disregard the thin layer that stays in motion beyond the front (above the green dashed line in Fig. 3f). Indeed, the mass never wholly stops in the Navier-Stokes code Basilisk in the inclined case. The drops beyond the front that still move after 1.02 s are thin and slow and continue flowing until the end of the simulated time (here $t = 2$ s). In the discrete model, the stopping phase starts at $t = 6$ s (Fig. 3g), and the mass never entirely stops during the calculation time, as continuous rearrangements keep occurring behind the front. This is not the case when smaller inclinations are considered (see Section IV A).

In all simulations, the final front position is each time in good agreement with the final front position from experiments (compare black squares and green dashed lines in Fig. 3). For $\theta = 0°$, the front stops at similar times in experiments, discrete and Navier-Stokes simulations (0.45 s), while the front stops sooner in thin-layer simulations (0.32 s). However, for $\theta = 16°$, the front stops at 0.64 s, but simulated fronts stop later: 0.93 s for the thin-layer model, 1.05 s for the Navier-Stokes model, and 6 s for the discrete model.

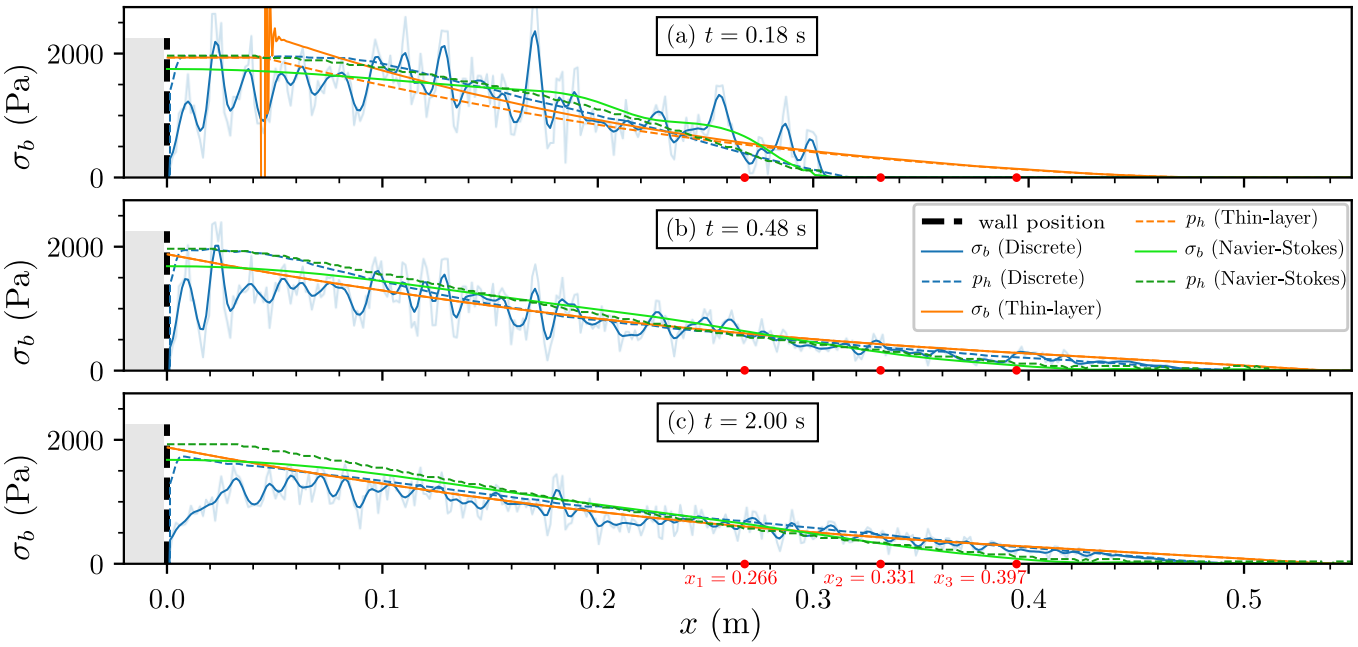

FIG. 5. Basal normal stress and hydrostatic pressure for $\theta = 0°$. (a) $t = 0.18$ s, (b) $t = 0.48$ s, (c) $t = 1.99$ s. For each simulation, we compute the basal normal stress σ_b, and the hydrostatic pressure p_h. The light blue, respectively dark blue, curve is the raw, respectively smoothed, normal stress derived from discrete COCD simulations. See Appendix B 3 for details on computation. The gray light at the right of the wall limit (dashed black line) represent the left wall.

4. *Velocity field and static/flowing interface in discrete and Navier-Stokes models*

The evolution of the horizontal velocity norm through the depth of the flow and during the collapse, $|V_x(z,t)|$ is shown in Fig. 4 for $\theta = 0°$. This information can only be obtained using the discrete and Navier-Stokes models since the velocity is depth-averaged in the thin-layer, one-layer model considered here. The static/flowing transition is defined by considering a velocity threshold of 1 cm s^{-1}, as in the previous section and in [17].

Fig. 4a and Fig. 4e, corresponding to $t = 0.15$ s, are snapshots of the velocity field during the acceleration phase for the Navier-Stokes and the discrete models. During this phase, the horizontal velocities obtained with the two models are similar (compare the colors). The static/flowing interfaces also have a similar shape (red dashed line).

Fig.4b and Fig.4f, at $t = 0.30$ s, correspond to the deceleration phase for both simulations (the flow front has started to slow down). Although velocities are comparable, the moving part inside the column is larger in the discrete simulation. In particular, the horizontal length of the flowing domain, behind the flow front, is 12 cm for the Navier-Stokes (Fig. 4b) and 20 cm for the discrete model (Fig. 4f).

We observe notable differences between the Navier-Stokes model (Fig. 4c and d) and the discrete model (Fig. 4g and h) during the stopping phase even though similar profiles of the deposit are obtained. The static/flowing interface propagates from the front to the left and from the bottom to the free surface for the discrete code (see the evolution of the red dotted line between $t = 0.5$ s and 0.8 s (Fig. 4g, h). For the Navier-Stokes simulations, the front is always moving and the static/flowing interface goes up uniformly from the bottom towards the free surface between $t = 0.5$ and 0.8 s (Fig. 4c, d).

The discrete simulation shows deeper rearrangements than for the Navier-Stokes model, even after the flow front has stopped. Indeed, motion occurs 4 cm below the free surface at $t = 0.5$ s with velocities locally higher than 0.35 m s^{-1} (Fig. 4g). At $t = 0.8$ s (Fig. 4h), velocities are below 0.25 m s^{-1}, but motion still occurs 3 cm below the surface. We can clearly identify in Fig. 4h the progression of the stopping wave that propagates from the flow front towards the rear.

C. Basal stress

1. *Spatial variations*

The basal normal stress σ_b and hydrostatic pressure p_h derived from the three codes are represented along with the domain in Fig. 5 for $\theta = 0°$, at three different times: $t = 0.18$ s, $t = 0.48$ s and $t = 2.0$ s, where the flow is at rest in the three simulations (see the corresponding mass profiles at these times in Fig. 2c) The basal stress σ_b is the stress applied to the bottom by the mass. It

may differ from the hydrostatic pressure p_h related to the weight of the granular column on the bottom. The way σ_b and p_h are computed in each code is described in Appendix B 3.

The stresses σ_b and pressures p_h computed from the discrete and Navier-Stokes models are in good agreement for $x \geq 0.2$ m (*i.e.*, at the right of the initial gate, see Figs. 5 a,b, and c) even though σ_b is much smoother in the Navier-Stokes model.

The thin-layer model compares well with the others except for $t = 0.18$ s (Fig. 5a), where its front is too far (0.48 m in the thin-layer model against 0.31 m for the others). As already mentioned in Section III A, it is because the flow propagates faster in thin-layer models. The other difference is a perturbation observed at $t = 0.18$ s and $x = 0.045$ m in the stress σ_b (discussed in Section IV B).

Significant variations in discrete simulation of σ_b are observed around the average values calculated in the other codes (compare blue line to other curves in Fig. 5a,b,c). These oscillations have amplitudes up to 75% of the mean value computed with the other codes at $t = 0.18$ s, while they account only for 50% of it at $t = 0.48$ s (Fig. 5b), and 20% at $t = 2.0$ s (Fig. 5c), when the flow is at rest. These oscillations are expected. Note that the more spatially smoothed the stress curve of the discrete model is, the closer it is to that of the other two models.

For $x \leq 0.2$ m, we observe significant discrepancies between the different values of σ_b and p_h. For instance, the basal normal stress σ_b derived from discrete simulations is about 50% lower than the hydrostatic pressure p_h derived from the same simulation (compare blue plain lines and blue dashed lines in Fig. 5). Interestingly, Fig. 5 also shows that the stress applied on the bottom in the Navier-Stokes model can be different from the hydrostatic pressure. For instance, for $x \simeq 0.15$ m at $t = 0.18$ s, the basal normal stress is smaller than hydrostatic and, around $x \simeq 0.15$ m, it gets higher, see Fig. 5a. The Navier-Stokes normal stress σ_b also varies less in space, leading to smaller pressure gradients and thus smaller driving forces than those based on hydrostatic pressure in thin-layer models.

2. *Temporal variation*

In Fig. 6, we compare the temporal variation of stress σ_b and pressure p_h at three different locations (see caption of Fig. 6) for $\theta = 0°$ and $\theta = 16°$. For each slope, the locations of probes x_1, x_2 and x_3 correspond respectively to 25%, 50%, and 75% of the runout distance from the gate. For example, the probes locations are represented by red dots in Fig. 5c. Fig. 6 also shows the basal pressure, denoted P, for Navier-Stokes model Basilisk (khaki line), measured in the first cell above the bottom boundary layer.

The time at which the mass front reaches the probes is the minimal time with a non-zero stress signal. This time is shorter for thin-layer models than for the two others that are equal (Fig. 6). The difference is approximately about 1 s for x_1 and x_2 (Fig. 6a,b,d,e) but may differ for x_3 (Fig. 6c,f). Another characteristic time is the duration needed by the mass to reach its local maximal height. It can be measured in Fig. 6 by the the duration between the time where the front reach the probe and the time at which the hydrostatic pressure is maximal. This duration is longer for thin-layer and Navier-Stokes models in the inclined case than for the horizontal plane. It is 0.06 s (Fig. 6a) against 0.2 s (Fig. 6d) for Navier-Stokes and 0.26 s (Fig. 6a) against 0.40 s (Fig. 6d). While discrete model is between them for $\theta = 16°$ (0.35 s (Fig. 6d)) it is much longer for the horizontal plane (0.75 s (Fig. 6a)).

For $\theta = 0°$, Fig. 6 shows that normal stress σ_b and pressure P are very close, except for the flow at high velocities (compare green and khaki lines for $t \in [0.2, 0.4]$ s in Fig. 6a). They are obviously equal when the mass is at rest, $t \geq 2$ s (Figs. 6a-c). Additional stress variations appear in the Navier-Stokes model compared to the thin-layer model (see, *e.g.*, Fig. 6a). However, these variations are still much smaller and at much longer periods than the stress fluctuations calculated with the discrete model. At a given probe, the local stress computed by discrete model can be completely different from the hydrostatic pressure, as expected (see σ_b for $t \geq 0.8$ s in Fig. 6a and Fig. 6c).

The basal stresses simulated with the continuum models (thin-layer and Navier-Stokes) at $\theta = 16°$ are smaller than for $\theta = 0°$ for the same position to the front (compare Figs. 6a with 6d, 6b with 6e, and 6d with 6f (75%)). Note that the instabilities of SHALTOP and Basilisk, already observed for $\theta = 0°$ and probe x_1 (see figure (6a)), are also visible for $\theta = 16°$ and probes x_1, x_2 and x_3, (see Fig. 6d-f).

The behaviour is more complex when looking at discrete simulations. Indeed, in that case, the basal stress fluctuations are much higher at $\theta = 16°$ than at $\theta = 0°$. For the discrete model COCD, Figs. 6b and Figs. 6d clearly show that the basal stress can be almost two times higher or lower than the hydrostatic pressure. Indeed, in discrete simulations, when the mass is almost at rest for $t \geq 0.8$ s, σ_b can be close to p_h (Figs. 6d, e, f), lower than p_h (Figs. 6a), or higher than p_h (Figs. 6b, c).

IV. DISCUSSION

A. Differences in flow dynamics

The discussion focus here on the three different phases defined in Section III B: the *acceleration*, the *deceleration*, and *stopping* phases.

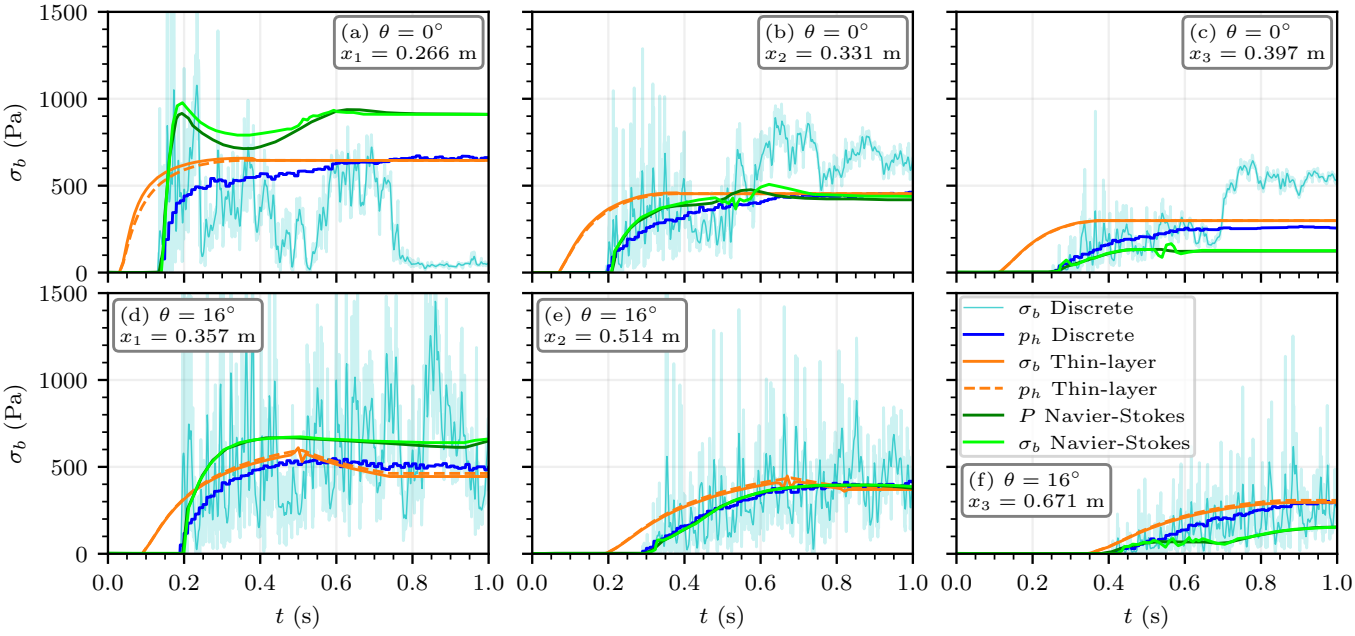

FIG. 6. Time evolution of basal normal stress σ_b (and hydrostatic pressure p_h for the discrete model) at three different probes, for $\theta = 0°$ (first row, a-c), and $\theta = 16°$ (second row, d-f). For $\theta = 0°$ (resp. $16°$), the probes positions are $x_1 = 0.266$ m (a), $x_2 = 0.331$ m (b), and $x_3 = 0.397$ m (c) (resp. $x_1 = 0.357$ m (d), $x_2 = 0.514$ m (e), and $x_3 = 0.671$ m (f)). These probes locations respectively correspond to 25%, 50%, and 75% of the distance between the runout distance and the gate position ($x = 0.2$ m). For discrete σ_b, the light blue, (resp. dark blue) curve is the raw (resp. smoothed), basal normal stress.

1. *Flow initiation (acceleration phase)*

The flow initiation is quantitatively similar for the Navier-Stokes model Basilisk and the discrete model COCD (Figs. 2, 3, 4). During this initiation, the profiles obtained with the two codes slightly differ from the experiments from [17] (see Fig. 2a, d). This may be due to the presence of a gate in experiments, where the release is fast but not instantaneous [31]. The thin-layer model SHALTOP overestimates the initial spreading with higher velocities than the others (compare Fig. 3a with Fig. 3b, c, and Fig. 3d with Fig. 3e, f). This well-known behavior of such models [55, 75] is due to non-negligible vertical velocities/accelerations leading to non-hydrostatic pressure inside the granular column, which contradicts the thin-layer approximation (*e.g.*, figure 12 in [85]). Furthermore, the analytical solution of the dam-break problem, described by thin-layer equations with constant friction coefficient smaller than the tangent of the bed slope, shows that the front velocity in these models is maximum at $t = 0$ s (see [79] and equation (3) in [16]). This is consistent with our simulations where the acceleration phase is less than 0.02 s (when outputs are written every 0.01 s), although in our case the friction coefficient is not constant and is higher than the slope bed.

These behaviors are qualitatively similar for $\theta = 0°$ and $\theta = 16°$. The duration of the acceleration phases simulated by the discrete and Navier-Stokes models does not depend much on the slope (between 0.20 and 0.24 s for both $\theta = 0°$ and $\theta = 16°$). This is coherent with laboratory experiments (see location of the curves maximums in figure 9b in [16]).

2. *Deceleration phase*

The deceleration phases are quantitatively similar for the Navier-Stokes and discrete models COCD (Figs. 2a,d, Figs. 3b,c, 3e,f, and Figs. 4b,f). Differences are observed near the front where some drops and bubbles appear in Basilisk as numerical artifacts at $\theta = 16°$. These artifacts are due to Basilisk's flow description. Indeed, as grains and air are both described as incompressible materials, the process of bubble formation and dynamics is not physically appropriate in the model. These instabilities get stronger as the slope angle increases due to increased flow front velocity.

However, the stopping "waves" initiation behavior is in qualitatively good agreement between the three models. Indeed, for all of them, the stopping "waves" start at times close to the stopping of the front at $\theta = 0°$ (Figs. (3a,b,c)) while they start at the left wall before the front stopping at $\theta = 16°$ (Figs. (3d,e,f)), even though this is less clear for the Navier-Stokes model.

3. *Stopping phase*

The spatio-temporal characteristics of the stopping phase are different in the three models. The thin-layer model stopping phase is the fastest since at $\theta = 0°$ the whole mass stops shortly after the front and at $\theta = 16°$ the front is the last part of the mass to stop (Figs. 3a,d). Indeed, a flow column will stop as soon as driving forces related to inertia, gravity and surface slope drop below $gh\cos(\theta)\mu(I)$. Thus, contrary to Basilisk and COCD models, vertically distributed movement (where the base of the flow is at rest but its top is still moving) is not modelled. However, even if the surface flows are expected to slightly remodel the deposit shape, the deposits obtained by SHALTOP are in excellent agreement with experiments, especially for the inclined plane, see Fig. 2f. Indeed, as the slope angle increases, the flow gets thinner and therefore is better suited to be described by the thin-layer approximation.

The longest stopping phase is with the COCD, see Figs. (3b,e). At $\theta = 0°$, the stopping wave, initiated at the front and propagating backwards (see Figs. 3b and 4g,h) is in good qualitative agreement with the 3D granular collapse experiments of similar aspect ratio (see section 4.2 of [55]). The most significant difference with the experiment is observed for the discrete model at $\theta = 16°$, where the flow is still moving after 1 s, (Fig. 2f), and stops after $t = 6.3$ s, (Fig. 3g). This large delay before the mass stopping at $\theta = 16°$ is due to the 2D configuration (see Section IV E).

Finally, the time delay between the initiation of the stopping and the full stopping of the mass in the Navier-Stokes model is in between the time delay obtained with the other models at $\theta = 0°$, (Fig. 3c) and similar to the thin-layer model at $\theta = 16°$. The Navier-Stokes model provides the closest deposits to the experiments, see Fig. 2. Interestingly, for $\theta = 0°$, it is the unique model that generates three stopping "waves," see Fig. (3c). However, a thin layer (lower than 3.5 mm) is still in motion at a low velocity (between 1 and 3 cm. s^{-1}) for $t \geq 1.2$ s, see Fig. 3f. Indeed, as a maximum viscosity is imposed in Basilisk, the mass never really stops. Prescribing a maximum viscosity is equivalent to regularisation methods (*e.g.,* [30]). Increasing the maximum viscosity which would lead to better deal with the yield behaviour (stopping) significantly increases the computation time. Optimal values of the maximum viscosity should be found by numerical analysis that compares the regularization error with the spatial discretization error (Section 5.2 in [33]).

The stopping phase appears to have excellent characteristics to discriminate the models and, in particular, the appropriate rheological laws. Thus, qualitative and quantitative comparison with the stopping phase observed in laboratory experiments would be very interesting (*e.g.*, section 4.4 and figure 4 of [86]), but we do not have such data for these experiments. Indeed, contrary to flow profiles, accessing measurements inside the moving granular mass to study the stopping phase is technically challenging in experiments.

B. Differences in basal stresses

A significant part of the basal stress results from the weight of the granular column (*i.e.,* hydrostatic pressure) for all three models, see Figs. (5b, c) for $x \geq 0.2$ m. Consequently, the difference between the absolute positions of the curves, related to the different models, is mainly due to the different local mass thicknesses. It explains why the basal normal stresses obtained with the three models are in good quantitative agreement if the free surfaces are similar at a given position.

As the increase of bed inclination favors mass spreading, flow thickness is reduced. Thus, the weight of the grains is smaller at $\theta = 16°$ than at $\theta = 0°$. It is why the basal stresses simulated with the continuum models (thin-layer and Navier-Stokes) at $\theta = 16°$ are much smaller than at $\theta = 0°$ despite higher velocities (compare Figs. 6a with d, b with e, and c with d). The perturbation that appears in the basal stress σ_b with the thin-layer model at $\theta = 16°$ can be directly associated with the formal expression of p_b in SHALTOP (see Eq. (B7)). The spatial derivatives of the velocity result in numerical artifacts since the velocity is not twice differentiable at the static/flowing transition.

In the Navier-Stokes simulation, the basal normal stress σ_b may be different from the hydrostatic pressure p_h (Fig.5a), but is relatively similar to the pressure P, indicating that deviatoric stresses are small (Fig. 6). When $\sigma_b \geq p_h$, a significant vertical motion induces a higher basal stress than the hydrostatic pressure. However, it is not clear how the stress σ_b can be lower than p_h. However, it is similar to what is observed in simulations obtained with the discrete model.

The most crucial difference for basal normal stresses is between the continuum and discrete models. Indeed, the discrete basal stress depends on the dynamics of colliding beads and on the geometry of the granular lattice varying with both space and time, see [87]. The discrete stress σ_b highly fluctuates around the hydrostatic pressure p_h (Fig. 5 and Fig. 6). During the flow, multiple grain rearrangements change force chains distribution within the granular media leading to strong variations in the basal stress: as a result, a small surface at the bottom of the flow may well carry more, or less, than the weight of the granular column of grains above it. These stress fluctuations increase with the slope (compare the two rows in Fig. 6). It is consistent with experiments and models discussed in [43], showing that the ratio between force fluctuations and the mean force at the base of granular flows increases with increasing inertial number I. These fluctuations decrease during the stopping phase (Fig. 5). Indeed, as successive collisions progressively dissipate energy with time, σ_b depends more and more on the static distribution of weight

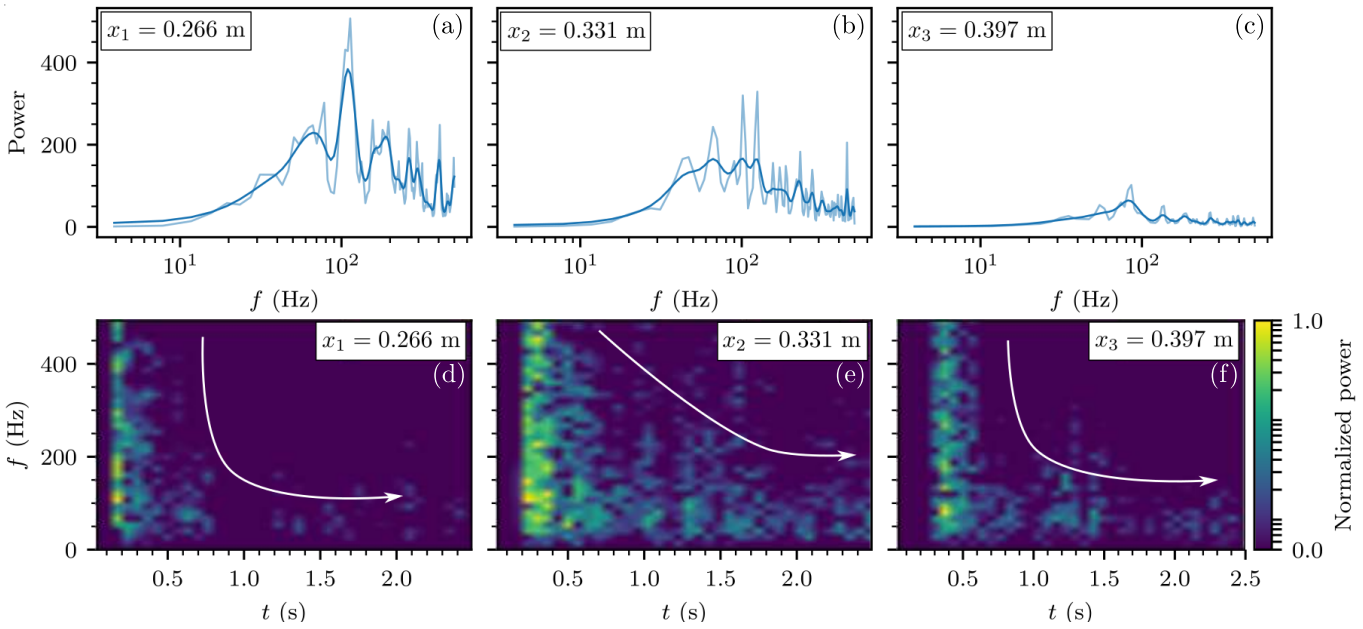

FIG. 7. Spectral content of the discrete (COCD) basal normal stress σ_b at $\theta = 0^\circ$ computed at $x_1 = 0.27$ m (a,d), $x_2 = 0.33$ m (b,e) and $x_3 = 0.40$ m (c,f). The first line (a-c) is the spectral amplitude (light blue line: raw Fourier transform, dark blue line: smoothed Fourier transform). The second line (d-f) displays the corresponding spectrograms. The associated signals are given in Fig. 6.

through the granular lattice and associated force chains, rather than on dynamics contributions.

Another specific point in discrete model simulations is the decrease of σ_b close to the left wall (see Fig. 5). It is similar to the Janssen effect in a grain silo, where the stress is far from the hydrostatic pressure at the silo's bottom. Indeed, part of the granular weight is supported by the lateral walls [88, 89]. In this simulation, the domain left wall contributes to handling part of the granular weight that is not applied on the bottom. This particular stress profile can also be explained by the construction history of the granular column that strongly affects static stress distributions, as shown by [87] for a granular pile.

C. Spectral analysis of discrete basal normal stress

Section III C 2 shows that σ_b calculated from discrete simulations (COCD) displayed much higher temporal variations than continuum simulations. Here, we analyze the spectral content of the basal stress as displayed in Figs. (7a-c) showing its spectrogram at the different probes x_i, $i = 1, 2, 3$ for $\theta = 0^\circ$. More precisely, we only consider here the fluctuations in the signals by substracting the smooth signal (the dark-blue line) from the total signal (light-blue line) in Fig. 6. Figs. (7d, e, f) are the spectrograms of these signals. The maximum frequency that can be measured here is 500 Hz, related to the time step of the discrete simulation ($\Delta t = 0.001$ s). Acoustic measurements of waves generated by steady granular flows or column collapses show that wave frequencies go up to ten's of kHz in our conditions, see [41–43]. These frequencies are related to the Hertz contact, not accounted for in our Contact Dynamics framework simulations.

The main frequency observed is around 100 Hz for the three probes (Fig. 7a-c), and the maximum frequency decreases as the distance of the probe increases and with time (Fig. 7d-f). The range of dominant frequencies (with an associated power higher than 150 in Fig. 7a) is 35-300 Hz. The corresponding periods (0.003-028 s) may correspond to the characteristic times t_{macro} for grain rearrangements due to the average shear between layers of grains, see Eq. (6.3) in [1]. For the three probes, Fig. 8 presents the mean frequency of layer frequencies $f_{ij} = 1/t_{\text{macro},ij}$ related to the characteristic time $t_{\text{macro},ij}$ related to the shear of layers in the mass thickness. More precisely, $t_{\text{macro},ij} = d/|\Delta u_{ij}|$, $i < j$ where d is the mean grain diameter, and Δu_{ij} is the relative velocity between two connected layers (see details of its computation in Appendix B 3). Fig. 8 shows that this mean frequency belongs to the range of dominant frequencies mentioned before. It enforces the hypothesis that the main event during the flow is related to the time t_{macro}, corresponding here to the average time for one bead from layer j to pass over one another bead from layer i. Further studies are needed to explore this hypothesis.

The total radiated energy decreases from the first to the third probe, probably because energy is progressively dissipated within the granular media. Lab-experiments

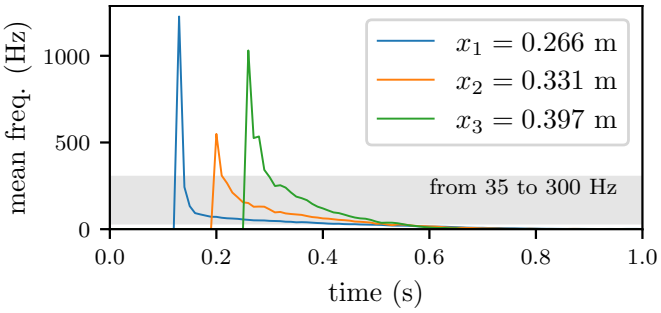

FIG. 8. For the three probes, the mean frequency of frequencies f_{ij} related to characteristic times $f_{ij} = 1/t_{\text{macro},ij}$ related to the shear of layers i, j in the mass thickness (see details of this computation in Appendix B 3).

of granular collapses and generated acoustic waves showed that the radiated energy decreases before the deceleration phase of the front (see Fig. (8a,b) of [41]). The deceleration phase at $\theta = 0°$ is starting around 0.2 s here, so that when the front arrives at probes x_2 and x_3 it has already decelerated.

The spectrograms (Fig. 7d-f) highlight that most energy is radiated when the flow front reaches the probes, at times $t = 0.1$, 0.2, and 0.3 s for x_1, x_2, and x_3. One can distinguish two behaviors: for x_1 and x_3, (Fig. 7d and 7f), most of the energy is radiated in the first 0.3 to 0.4 s after the front arrives. The associated frequency bandwidth is 30-400 Hz, with main frequencies between 100 and 200 Hz. Afterwards, generated frequencies hardly exceed 175 or 200 Hz. On the contrary for x_2, in the first 0.3 s following the front arrival, energy is almost evenly distributed over the 30-300 Hz frequency bandwidth (Fig. 7e). Besides, contrary to the other probes, the decrease in energy radiation and frequency bandwidth is more progressive and lasts more than 1 s (compare white arrows in Fig. 7d-f).

The behavior at x_2 compared to x_1, and x_3 may be explained by the fact that the flow is more transient at x_1 (quick acceleration near the initial mass) and x_3 (flow stop quickly after arrival), than at x_2 where the flow decelerates progressively. Furthermore, at x_1, after the front passes, the grains near the base are almost static and the moving grains near the free surface are far from the base (see Fig. 4e-h) so that the stress fluctuations from the upper grains hardly reach the base. For x_3, at $t = 0.5$ s there is almost no moving grains above the front so that the stress fluctuation decreases rapidly (see Fig. 3b). Then x_2 has an intermediate behavior. Indeed, at this position, the grains near the free surface are still moving until about 0.8 s (Fig. 4h) and, as the flow thickness is quite small at this position (around 2.5 cm corresponding to ~ 3 beads, Fig. 2b), the associated stress fluctuations may propagate down to the base during the relaxation phase of the upper grains up to full stopping of the mass. However, given the strong spatial variation of the basal normal stress and the role of force chains in the stress transmission, a deeper analysis of these processes should be performed which is beyond the scope of this paper.

The spectrograms in Fig. 7 can be qualitatively compared to those obtained in laboratory experiments, from bottom force measured at the arrival of an avalanche at a given location (see Fig. 3a of [43]). In these measurements, the front arrival signature is similar to that calculated here, even if their dominant frequencies are much higher. The spectrogram at probe x_2 in our study (Fig. 7e) is closer to the experimental spectrogram which have been measured for a granular mass reaching a steady-uniform regime some time after the front arrival.

Note that a pulse of energy can be observed at all probes at about 1.1-1.4 s, more visible at x_3 (Fig. 7f). This regain of radiated energy is related to the full stopping of the mass as can be seen in Fig. 3b.

D. Influence of rheological parameters

1. *Rheological parameters for the rheology in continuum simulations*

In order to compare the different models considered in this work, we chose a set of parameters that proved to reproduce rather correctly the evolution of the column collapse free surface in the case $\theta = 0°$. However, the determination of appropriate rheology for granular flow modeling and the choice of corresponding rheological parameters are still open issues.

Considering the $\mu(I)$-rheology for the column collapse simulations, several values of μ_1, μ_2 and I_0 can be found in the literature, all being specifically defined either in experimental or numerical studies. For instance Jop *et al.* [73] measure experimentally

$$\mathcal{R}_{\text{Jop}} = \{\mu_1 = 0.382, \quad \mu_2 = 0.644, \quad I_0 = 0.279\}, \quad (17)$$

whereas [90] obtained, by calibrating $\mu(I)$ with axisymmetric DEM simulations, that the best fit to their data was

$$\mathcal{R}_{\text{Lac}} = \{\mu_1 = 0.40, \quad \mu_2 = 0.70, \quad I_0 = 0.3\}, \quad (18)$$

and [30] choose

$$\mathcal{R}_{\text{Lag}} = \{\mu_1 = 0.32, \quad \mu_2 = 0.60, \quad I_0 = 0.4\}, \quad (19)$$

to match the results obtain with the Navier-Stokes Gerri's flow solver to 2D-DEM simulations. Based on a previous study comparing numerical simulations to experimental column collapse, [31] defined the friction parameters in their continuous models as

$$\mathcal{R}_{\text{Ion}} = \{\mu_1 = 0.480, \quad \Delta\mu = 0.250, \quad I_0 = 0.279\}. \quad (20)$$

These last coefficients have explicitly been defined to match the experimental data of [16] by increasing the static friction coefficient μ_1 to consider the effect of the

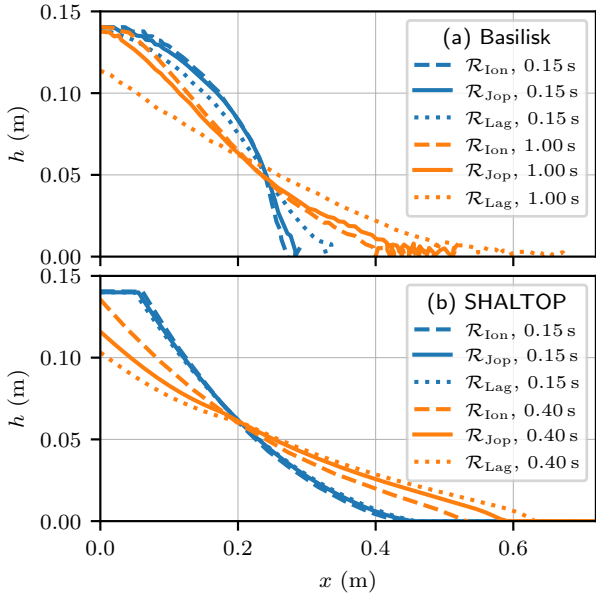

FIG. 9. Influence of $\mu(I)$-rheology parameters on simulation results, for $a = 0.7$ and $\theta = 0°$. We display flow profiles at $t = 0.4$ s and $t = 1.0$ s. (a) Basilisk simulations with parameters from [31] (used in previous figures, $\mathcal{R}_{\mathrm{Ion}}$), parameters from [73] ($\mathcal{R}_{\mathrm{Jop}}$), and from [30] ($\mathcal{R}_{\mathrm{Lag}}$). (a) SHALTOP simulations with parameters $\mathcal{R}_{\mathrm{Ion}}$, $\mathcal{R}_{\mathrm{Jop}}$, and $\mathcal{R}_{\mathrm{Lag}}$.

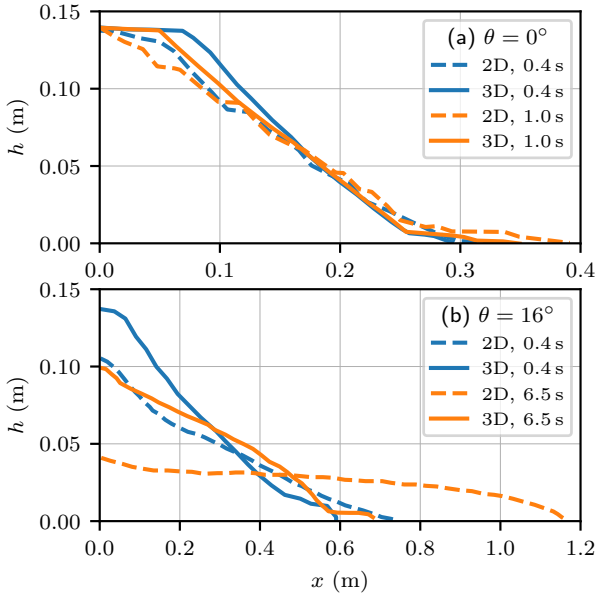

FIG. 10. Influence of the space dimension on the discrete model COCD results, for $\theta = 0°$ (a) and $\theta = 16°$ (b). The aspect ratio is $a = 0.7$. The friction coefficient is exactly the same between the 2D and 3D simulations, $\mu_p = 0.9$. We display flow profiles at $t = 0.4$, 1.0, and 6.5 s. At $\theta = 16°$ (b), the 3D simulation is at rest at 1.63 s.

lateral walls on the spreading of the granular column. Indeed, at the moment, the frictional dissipation due to lateral walls cannot be taken into account otherwise in 2D simulations.

To better evaluate the effect of the frictional coefficients in the $\mu(I)$-rheology, a comparison between $\mathcal{R}_{Ion}$, $\mathcal{R}_{Jop}$ and $\mathcal{R}_{Lag}$ is presented in Fig. 9. As expected, the lower the friction coefficients, the longer the runout distance. The longest is obtained using $\mathcal{R}_{Lag}$, then $\mathcal{R}_{Jop}$ and finally $\mathcal{R}_{Ion}$. However, note that the initial dynamics are relatively similar, at least during the first 0.15 s. It suggests that the differences between the thin-layer and Navier-Stokes dynamics may be still qualitatively similar to those analysed in this study for a wide range of parameters.

2. *Friction coefficient in discrete COCD simulations*

In discrete simulations, it is also non-trivial to choose the friction coefficient. In [91], a table with values used in the literature is given: they range between $\mu_p = 0$ and $\mu_p = 1$. The influence of the friction coefficient in COCD simulations can be found in figure 5 of [51]: it obviously shows that the smaller the coefficient of friction, the greater the distance reached by the front. However, the difference is small (about 15% between $\mu = 0.2$ and 0.8), especially compared to the influence of the 2D versus 3D discrete simulations (see Section IV E).

E. Influence of simulation geometry

In this work, we have considered that the granular flow dynamics does not change in the direction transverse to the flow. As discussed in the previous section, it is not true in reality, as lateral walls can have a significant impact on the flow [31]. This effect is oversimplified here and tackled by empirically increasing friction coefficients of the $\mu(I)$ rheology in continuum models (see *e.g.*, [32] for wall effects).

As explained in Appendix A, SHALTOP's implementation does not solve the thin-layer equations in a 2D domain, and we have to solve them in a 3D domain. That is, we solve for the depth-averaged velocity field $\bar{V}_x(x, y, t)$ in a channel of arbitrary width W and use lateral boundary conditions and initial conditions to ensure that $\bar{V}_x$ does not depend on y. With this method, SHALTOP proved to reproduce the 2D thin-layer dam-break problem's analytical solution accurately. Thus, we can be confident that our simulation results do not depend on the width W of the channel used in simulation and are consistent with the 2D thin-layer equations.

In COCD simulations, the 2D equations describe the motion of discs, whereas the 3D equations describe the motion of spheres. Fig. 10 shows that with the same friction coefficient μ_p, the repose angle is smaller in 2D than in 3D. For example, in [51], the maximal avalanche angle for 2D flows is about 17° when considering $H_0/d = 15$, with d the mean diameter of grains while it is above

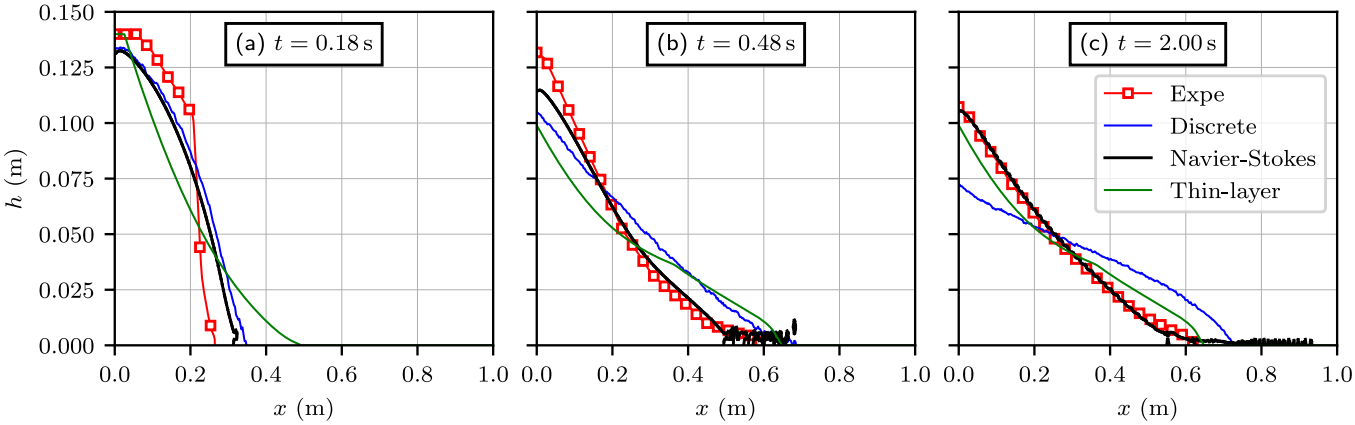

FIG. 11. Comparison between experiments and numerical simulations of the granular profiles during a column collapse. We display the experiment results (red squares), discret COCD simulations (blue line), Navier-Stokes Basilisk simulations (black line) and thin-layer SHALTOP simulations (green line). The initial aspect ratio is $a = 0.7$, with a bed slope $\theta = 10°$ at times 0.18 (a), 0.48 (b), and 2 s (c). At $t = 2\,\mathrm{s}$ in (c), the three codes are at rest.

22° in 3D, as in experiments [16, 17]. The smaller value of the repose angle in 2D, compared to 3D, can be explained by the fact that in 3D, spheres can spread laterally, in the collapse transverse direction. It increases the number of potential traps but also the number of potential contacts, inducing a higher dissipation due to Coulomb friction between the grains. It explains, at least partly, why the friction coefficient we use in COCD simulations, $\mu_p = 0.9$ (see [51]), must be higher than the friction coefficient between glass spheres estimated from experiments ($0.2 \leq \mu \leq 0.3$), which is in the range between the friction coefficient measured for a perfect glass/glass contact $\mu = 0.4$ [69] and that measured with Molecular Dynamics models (MD) $\mu = 0.16$. Here, COCD runs in 2D because our goal is to compare the three models in the same 2D space configuration.

Here, we present the limit case for $\theta = 16°$ in 2D COCD simulations where the stopping is difficult but arises after a long duration (more than 6 s in Figs.3e and 10b). When considering a smaller inclination angle, the flow stops similarly to the two other models, see Fig. 11.

V. CONCLUSIONS

The comparison between discrete (COCD), Navier-Stokes (Basilisk), and thin-layer (SHALTOP) models for a simple granular column collapse simulation show that they can reproduce the profiles measured in lab-experiments with different level of accuracy, provided an appropriate choice of the rheological parameters is made. The $\mu(I)$ rheology is used here for both continuum models. The rheological parameter are kept constant for each model when simulating the granular collapses at three different angles from horizontal to $\theta = 16°$. Even if the differences between the models strongly depend on the rheological parameters and simulation setups, general conclusions could be made:

- The thin-layer model overestimates the initial acceleration and velocity compared to the other models and to the experiments, although the final deposits are consistent with the Navier-Stokes simulation with the same values of the $\mu(I)$ rheology (except the volume fraction Φ that has, however, only a limited influence on simulation results) and with the experiments.
- The Navier-Stokes and discrete simulations have the same acceleration and deceleration phases but differ in the stopping phase. After the front stops, more and deeper particles are still in motion in the discrete simulations. The thin-layer simulations are globally faster than the two others in the three phases.
- 2D simulations thus requires an artificially higher inter-particle friction coefficient when compared to 3D experiments (laterally confined flow here). In particular, in 2D discrete simulations using the same friction coefficient between the beads for slopes $\theta = 0°$ and $\theta = 16°$ results in a flow lasting several seconds too long at $\theta = 16°$.
- For $\theta = 16°$, the flow front is hardly managed in the Navier-Stokes code Basilisk with the apparition of artificial bubbles whose number increase as the slope angle increases.
- The basal normal stress measured from the Navier-Stokes and thin-layer models are qualitatively similar and mainly depend on the flow thickness even though slightly higher variations are simulated with the Navier-Stokes model which may be due to non-hydrostatic effects. The basal stress resulting from the discrete model is much more complex, with important spatial and temporal fluctuations at much higher frequencies, related to the grain-scale motion.

A key point is that the differences between the models are more visible at higher slope angle. Furthermore, the characteristics of the basal stress and of the stopping phase appear to be much more discriminant for the models and rheology than the mass profiles during the collapse. This strongly suggests to use these quantities and to consider the configuration of granular flows on sloping beds to assess the performance and limits of granular flow models and rheological laws or to calibrate the models. This is particularly important for modeling field-scale geophysical flows, when the simulated dynamics are compared to seismic recordings that give us a direct measurement of the basal stress applied by the landslide to the ground [46, 48, 92].

ACKNOWLEDGEMENTS

This work was funded by project ERC-CG-2013-PE10-617472 SLIDEQUAKES and Institut Universitaire de France.

Appendix A: Numerical set-up

1. Initial conditions

The construction of the initial mass is straightforward in the Basilisk and SHALTOP simulations because it boils down to defining the boundary of the initial mass. In COCD (like in any DEM simulation), generating an initial state is more complex. The position, size, and the number of beads must be defined. The way the initial column is built in COCD can strongly impact the initial forces distribution in the granular media [87]. Following [87], the initial arrangement of beads is constructed by simulating a uniform rain of beads (whose diameter follows a Gaussian distribution of mean $d = 0.7\,\mathrm{mm}$ and standard deviation $0.07\,\mathrm{mm}$). It allows obtaining a granular network with a quasi-hydrostatic pressure [87]. However, in our initial box, the basal stress is not equal to the hydrostatic pressure, in particular, close to the left wall, as shown in section III C.

In experiments, remark that the gate opening affects only the early stage of the collapse, as shown in [32]. Thus, in our simulations, we consider an instantaneous release of the initial granular mass (without accounting for the gate).

2. Boundary conditions

In COCD and Basilisk simulations, the beads and granular flow dynamics are solved directly in the 2D domain (x, z), and no lateral boundary conditions are needed. On the contrary, SHALTOP solves the depth-averaged mass and momentum equations for flows on general 2D-topographies $Z = Z(X, Y)$ in a fixed vertical cartesian frame and not on 1D-topographies $Z = Z(X)$. In order to mimic a 1D-topography problem, the topography is represented by an inclined plane of width $W = 3 \times dx$ in the Y direction, with dx the numerical cell size. The initial mass spans the width of the grid uniformly. Then, a non-penetration condition is set on the lateral boundaries of the grid, i.e., on $Y = 0$, $Y = W$.

A non-penetration condition is also used on $x = 0$ (or equivalently at $X = 0$ for SHALTOP) in all three codes. This condition is done explicitly in COCD's simulations through a vertical wall. This wall interacts with the particles with the same friction coefficient than for grain to grain contacts. In Basilisk and SHALTOP, we impose $V_x = 0$ and $\bar{V}_X = 0$, respectively.

The bottom boundary condition on $z = 0$ is specific to each code. In COCD's simulations, as in experiments, a glued layer of beads is added to the bed. The size distribution of these glued beads is identical to the other grains. There is no space between two consecutive glued beads. Even if this is not really true because the glued beads could not move (*e.g.* role), this can be seen as a no-slip and non-penetration condition, which is set explicitly in Basilisk ($V_x(z = 0) = 0$ and $V_z(z = 0) = 0$). Note that in Navier-Stokes simulation of the same set-up, [31] used a Coulomb friction condition at the base and studied the impact of this condition compared to the no-slip condition used here (see their figure 16 where deposit calculated with friction went about 0.04 m further than with no-slip). As SHALTOP solves directly for the depth-average velocity $\bar{V}_X$, the bottom boundary condition is included in the equations and does not need to be specified numerically.

Note that thin-layer equations (12) and (13) can be derived in two different manners. It is possible to use the no-slip condition and the internal $\mu(I)$-rheology as in the Basilisk code. However, the same final equations are derived if we assume a Coulomb solid friction law at the interface between the flow and the topography, with a friction coefficient given by $\mu(I)$ as in (11), and no condition on the bottom velocity (and thus on the velocity profile). See Chapter 1 in [93] for details.

Appendix B: Simulation output processing

To compare simulations, we extract key characteristics of the flow and we detail in this section how they are calculated in each code.

1. Flow height and front position

For COCD's profiles, we first decompose the horizontal domain in cells of size $d_x = 4d$, where $d = 0.7\,\mathrm{mm}$ is the mean diameters of grains. The flow height is then defined, in each cell, as the height of the top most beads. The front is computed with this same method without other post-process.

One of Basilisk's outputs is directly the air/granular media interface, represented in Fig. 2, from which the determination of the flow height $h(x,t)$ is straightforward. Determining the flow front position is not straightforward because small drops detach from the main mass (e.g., Fig. 2e). The $\mu(I)$-rheology is no longer capable of modeling their propagation correctly, which may generate numerical issues. Indeed, due to these drops, the classical definition of the front position:

$$\hat{x}_f(t) = \max\{x, h(x,t) > 0\}, \tag{B1}$$

does not yield an appropriate (i.e., physically relevant) position for the flow front. Instead, the front position $x_f(t)$ is given by the intersection of the x-axis with the tangent to the graph $z_t(x) = h(x,t)$, for $x = \tilde{x}_f(t)$. $\tilde{x}_f(t)$ is the last position for which the flow height is positive for all abscissas before $\tilde{x}_f(t)$:

$$\tilde{x}_f(t) = \max\{X : \forall x < X, h(x,t) > 0\}, \tag{B2}$$

In practice, before estimating the tangent, the graph $z_t(x) = h(x,t)$ is smoothed (with a Lowess smoothing algorithm [94]). At time t_i, $x_f(t_i)$ is considered as an outlier if

$$\left|\frac{x_f(t_i) - x_m(t_i)}{x_m(t_i)}\right| > 0.01 \tag{B3}$$

where

$$x_m(t_i) = 0.5(x_f(t_{i-1}) + x_f(t_{i+1})). \tag{B4}$$

If Equation (B3) is verified, then we set $x_f(t_i) = x_m(t_i)$. This rough filtering works because, in practice, we never had two outliers in a row.

In SHALTOP, the layer thickness $h(x,t)$ is directly given as a simulation result. The flow front $x_f(t)$ is then given by:

$$x_f(t) = \min\{x, h(x,t) < 5d\} \tag{B5}$$

where $d = 0.7\,\text{mm}$ is the mean diameter of beads in COCD's simulations.

2. Flow velocity and flow depth-integrated velocity

COCD computes every grain velocity. Let us consider the same domain decomposition described in section B 1. At a given time t, we define the 2D columns of width dx and height $h_{d_x}(x)$ for each cell and detect all the grains that belong to them. We then compute its horizontal mean velocity $\bar{V}_x(x,t)$ for each column, by averaging all the horizontal velocities of grains included in the column. The local horizontal velocity is the horizontal part of the velocity vectors of each grain.

Basilisk explicitly solves for the velocity field within the flow, that is, $V_x(x,z,t)$ and $V_z(x,z,t)$. The depth-averaged flow velocity in the x-direction $\bar{V}_x$ is then directly deduced following Eq. (13).

SHALTOP solves directly for the depth-averaged velocity $\bar{V}_x$, and no further processing is needed.

3. Basal stresses and pressures

For COCD, let us consider again the columns, introduced in precedent section B 2. The probes have the same length dx as the columns. Since the grains belonging to each column can be detected, the total mass of the column is the sum of the masses of grains. In the computing of any grain mass m_i, we multiply the volume of the disc i by the grain diameter d_i, and by the glass density $\rho = 2500\,\text{kg.m}^{-3}$. We finally define the hydrostatic pressure p_h as being the column weight divided by the length (it would be the surface in 3D) of the bottom column d_x.

The basal normal stress σ_b is directly deduced from the resulting normal force applied on a probe (i.e., the resulting normal force applied on the four glued grains belonging to this probe) divided by its surface. It can be directly computed from the simulations results that include every contact force for all contacts at any time.

In SHALTOP, the hydrostatic pressure at the bottom of the flow is given by

$$p_h^{SH} = \rho g \cos(\theta) h. \tag{B6}$$

It is derived from the inviscid Navier-Stokes equations integrated into the topography normal direction (i.e., along the z-axis), assuming that the stress tensor is $\sigma = -pI_3$ and that $V_z = 0$ at the bottom. Following [46] and [92] for more general cases where $\sigma \neq -pI_3$, p_h^{SH} is the leading term of the basal stress σ_b in the direction perpendicular to the topography. In order to get an accurate value of the basal stress, other terms from the asymptotic expansion must be included (see Eq. 3 in [46], Eq. 5 in [92]). In the case of a flow over an inclined plane, an accurate value is

$$p_b^{SH} = p_h^{SH} - \frac{\rho}{2}\left(\frac{\partial}{\partial t}\left(h^2\frac{\partial V_x}{\partial x}\right) + \frac{\partial}{\partial x}\left(h^2 V_x \frac{\partial V_x}{\partial x}\right)\right). \tag{B7}$$

$$\sigma_n = (\boldsymbol{\sigma}\boldsymbol{n})\cdot\boldsymbol{n} \tag{B8}$$

$$= \left(\begin{pmatrix}\eta_{eff}\dot{\gamma}_{xx} - p & \eta_{eff}\dot{\gamma}_{xy}\\ \eta_{eff}\dot{\gamma}_{xy} & \eta_{eff}\dot{\gamma}_{yy} - p\end{pmatrix}\begin{pmatrix}0\\-1\end{pmatrix}\right)\cdot\begin{pmatrix}0\\-1\end{pmatrix} \tag{B9}$$

$$\sigma_n = \eta_{eff}\frac{\partial v}{\partial y} - p \tag{B10}$$

with

$$\eta_{eff} = \frac{\mu(I)P}{|\dot{\gamma}|} \tag{B11}$$

Concerning the mean frequency presented in Fig. 8, it is computed as the average of multiple frequencies f_{ij}. We decompose the mass height in layers of width $3d$, with d, the mean diameter of grains. For each layer i, the mean along-slope velocity $u_{x,i}$ is computed in a horizontal range of size $20d$, centered in each probe position. It is

the velocity of grains belonging to layers of height $3d$ and horizontal size $20d$, centered in x_i, $i = 1, 2, 3$. We then compute the relative velocities between two successive layers $\Delta u_{ij} = u_{x,j} - u_{x,i}$, $j > i$ and the time $t_{\text{macro},ij}$ is then computed as

$$t_{\text{macro},ij} = \frac{d}{|\Delta u_{ij}|}.$$

By definition, $t_{\text{macro},ij}$ corresponds to the duration needed for a grain from the above layer j to go over a grain in the layer below i. The definition can be found in [1] (Eq. (6.3)). Finally, the mean frequency presented in Fig. 8 is the average of frequencies $f_{ij} = 1/t_{\text{macro},ij}$.

Appendix C: Numerical parameters

[1] B. Andreotti, Y. Forterre, and O. Pouliquen, *Granular Media: Between Fluid and Solid* (Cambridge University Press, 2013).

[2] J. L. Baker, C. G. Johnson, and J. M. N. T. Gray, Segregation-induced finger formation in granular free-surface flows, Journal of Fluid Mechanics **809**, 168 (2016).

[3] C. Hibert, A. Mangeney, G. Grandjean, and N. Shapiro, Slope instabilities in dolomieu crater, réunion island: From seismic signals to rockfall characteristics, Journal of Geophysical Research: Earth Surface **116** (2011).

[4] R. Delannay, A. Valance, A. Mangeney, O. Roche, and P. Richard, Granular and particle-laden flows: from laboratory experiments to field observations, Journal of Physics D: Applied Physics **50**, 053001 (2017).

[5] D. Hantz, J. Corominas, G. B. Crosta, and M. Jaboyedoff, Definitions and Concepts for Quantitative Rockfall Hazard and Risk Analysis, Geosciences **11**, 158 (2021).

[6] O. Hungr, Rock avalanche occurrence, process and modelling, in *Landslides from Massive Rock Slope Failure*, NATO Science Series, edited by S. G. Evans, G. S. Mugnozza, A. Strom, and R. L. Hermanns (Springer Netherlands, Dordrecht, 2006) pp. 243–266.

[7] A. Strom and K. Abdrakhmatov, Quantitative Relationships of Central Asian Bedrock Landslide Parameters, in *Rockslides and Rock Avalanches of Central Asia* (Elsevier, 2018) pp. 335–347.

[8] M. Peruzzetto, J. C. Komorowski, A. Le Friant, M. Rosas-Carbajal, A. Mangeney, and Y. Legendre, Modeling of partial dome collapse of La Soufrière of Guadeloupe volcano: implications for hazard assessment and monitoring, Scientific Reports **9**, 1 (2019).

[9] T. Esposti Ongaro, M. Cerminara, S. J. Charbonnier, G. Lube, and G. A. Valentine, A framework for validation and benchmarking of pyroclastic current models, Bulletin of Volcanology **82**, 51 (2020).

[10] V. Gueugneau, S. Charbonnier, T. Esposti Ongaro, M. Peruzzetto, A. Mangeney, F. Bouchut, A. Patra, K. Kelfoun, *et al.*, Synthetic benchmarking of concentrated pyroclastic current models, Bulletin of Volcanology **83**, 1 (2021).

[11] O. Korup, D. Schneider, C. Huggel, and A. Dufresne, Long-Runout Landslides, in *Treatise on Geomorphology* (Elsevier, 2013) pp. 183–199.

[12] A. Lucas, A. Mangeney, and J. P. Ampuero, Frictional velocity-weakening in landslides on Earth and on other planetary bodies, Nature Communications **5**, 10.1038/ncomms4417 (2014).

[13] G. Félix and N. Thomas, Relation between dry granular flow regimes and morphology of deposits: formation of levées in pyroclastic deposits, Earth and Planetary Science Letters **221**, 197 (2004).

[14] A. N. Edwards, S. Viroulet, B. P. Kokelaar, and J. M. N. T. Gray, Formation of levees, troughs and elevated channels by avalanches on erodible slopes, Journal of Fluid Mechanics **823**, 278 (2017).

[15] F. M. Rocha, C. G. Johnson, and J. M. N. T. Gray, Self-channelisation and levee formation in monodisperse granular flows, Journal of Fluid Mechanics **876**, 591 (2019).

[16] A. Mangeney, O. Roche, O. Hungr, N. Mangold, G. Faccanoni, and A. Lucas, Erosion and mobility in granular collapse over sloping beds, Journal of Geophysical Research: Earth Surface 10.1029/2009JF001462 (2010).

[17] M. Farin, A. Mangeney, and O. Roche, Fundamental changes of granular flow dynamics, deposition, and erosion processes at high slope angles: insights from laboratory experiments, Journal of Geophysical Research: Earth Surface **119**, 504 (2014).

[18] A. Edwards, S. Viroulet, C. Johnson, and J. Gray, Erosion-deposition dynamics and long distance propagation of granular avalanches, Journal of Fluid Mechanics **915**, A9 (2021).

[19] Y. Forterre and O. Pouliquen, Stability analysis of rapid granular chute flows: formation of longitudinal vortices, Journal of Fluid Mechanics **467**, 361 (2002).

[20] A. Mangeney, F. Bouchut, N. Thomas, J.-P. Vilotte, and M.-O. Bristeau, Numerical modeling of self-channeling granular flows and of their levee-channel deposits, Journal of Geophysical Research: Earth Surface **112**, F02017 (2007).

[21] L. Lacaze and R. R. Kerswell, Axisymmetric granular collapse: A transient 3D flow test of viscoplasticity, Physical Review Letters **102**, 3 (2009).

[22] P. A. Cundall and O. D. L. Strack, A discrete numerical model for granular assemblies, Géotechnique **29**, 47 (1979).

[23] J. J. Moreau, Sorne numerical methods in multibody dynamics: application to granular materials, European Journal of Mechanics A/Solids **4**, 93 (1994).

[24] B. Maury, A time-stepping scheme for inelastic collisions, Numerische Mathematik **102**, 649 (2006).

[25] F. Radjai, J.-N. Roux, and A. Daouadji, Modeling granular materials: century-long research across scales, Journal of engineering mechanics **143**, 04017002 (2017).

[26] F. Radjaï and F. Dubois, *Discrete-element modeling of*

TABLE I. Values of numerical parameters.

description	**parameter**	**value(s)**
Discrete, COCD		
Beads mean diameter	d	0.7 mm
Beads diameter standard deviation	σ_d	0.07 mm
Number of beads at 0°, 10° and 16°	N	74,293
Friction coefficient	μ_p	0.9
Navier-Stokes, Basilisk		
Size of grid cells in x-direction	dx	2.7 mm
Size of grid cells in z-direction	dz	2.7 mm
Parameters for the $\mu(I)$-rheology	μ_1, μ_2, I_0	(0.48, 0.73, 0.279)
Thin-layer, SHALTOP		
Size of grid cells in horizontal direction	dX	0.6 mm
Parameters for the $\mu(I)$-rheology	μ_1, μ_2, I_0	(0.48, 0.73, 0.279)

granular materials (Wiley-Iste, 2011).

[27] L. Girolami, V. Hergault, G. Vinay, and A. Wachs, A three-dimensional discrete-grain model for the simulation of dam-break rectangular collapses: Comparison between numerical results and experiments, Granular Matter **14**, 381 (2012).

[28] C. R. K. Windows-Yule, D. R. Tunuguntla, and D. J. Parker, Numerical modelling of granular flows: A reality check, Computational Particle Mechanics **3**, 311 (2016).

[29] L. F. Orozco, J.-Y. Delenne, P. Sornay, and F. Radjai, Scaling behavior of particle breakage in granular flows inside rotating drums, Physical Review E **101**, 052904 (2020).

[30] P. Y. Lagrée, L. Staron, and S. Popinet, The granular column collapse as a continuum: Validity of a two-dimensional Navier-Stokes model with a μ(I)-rheology, Journal of Fluid Mechanics 10.1017/jfm.2011.335 (2011).

[31] I. R. Ionescu, A. Mangeney, F. Bouchut, and O. Roche, Viscoplastic modeling of granular column collapse with pressure-dependent rheology, J. of Non-Newtonian Fluid Mechanics **219**, 1 (2015).

[32] N. Martin, I. R. Ionescu, A. Mangeney, F. Bouchut, and M. Farin, Continuum viscoplastic simulation of a granular column collapse on large slopes: μ(I) rheology and lateral wall effects, Physics of Fluids **29**, 013301 (2017).

[33] C. Lusso, A. Ern, F. Bouchut, A. Mangeney, M. Farin, and O. Roche, Two-dimensional simulation by regularization of free surface viscoplastic flows with Drucker–Prager yield stress and application to granular collapse, Journal of Computational Physics **333**, 387 (2017).

[34] M. Pirulli, A. Leonardi, and C. Scavia, Comparison of depth-averaged and full-3D model for the benchmarking exercise on lanslide runout, Hong Kong , 14 (2018).

[35] A.-J.-C. Barré de Saint-Venant, Théorie du mouvement non permanent des eaux, avec application aux crues des rivières et à l'introduction des marées dans leur lit, Comptes rendus hebdomadaires des séances de l'Académie des sciences **LXXIII** (1871).

[36] R. F. Dressler, New Nonlinear Shallow-Flow Equations with Curvature, Journal of Hydraulic Research **16**, 205 (1978).

[37] S. B. Savage and K. Hutter, The dynamics of avalanches of granular materials from initiation to runout. Part I: Analysis, Acta Mechanica **86**, 201 (1991).

[38] S. McDougall, 2014 Canadian Geotechnical Colloquium: Landslide runout analysis — current practice and challenges, Canadian Geotechnical Journal **54**, 605 (2017).

[39] M. Pastor, K. Soga, S. McDougall, and J. S. H. Kwan, Review of Benchmarking Exercise on Landslide Runout Analysis 2018, Hong Kong , 65 (2018).

[40] M. Peruzzetto, C. Levy, Y. Thiery, G. Grandjean, A. Mangeney, A.-M. Lejeune, A. Nachbaur, Y. Legendre, B. Vittecoq, J.-M. Saurel, V. Clouard, T. Dewez, F. R. Fontaine, M. Mergili, S. Lagarde, J.-C. Komorowski, A. Le Friant, and A. Lemarchand, Simplified simulation of rock avalanches and subsequent debris flows with a single thin-layer model: Application to the Prêcheur river (Martinique, Lesser Antilles), Engineering Geology **296**, 106457 (2022).

[41] M. Farin, A. Mangeney, J. De Rosny, R. Toussaint, and P.-T. Trinh, Link between the dynamics of granular flows and the generated seismic signal: Insights from laboratory experiments, Journal of Geophysical Research: Earth Surface **123**, 1407 (2018).

[42] M. Farin, A. Mangeney, J. De Rosny, R. Toussaint, and P.-T. Trinh, Relations between the characteristics of granular column collapses and resultant high-frequency seismic signals, Journal of Geophysical Research: Earth Surface **124**, 2987 (2019).

[43] M. I. Arran, A. Mangeney, J. De Rosny, M. Farin, R. Toussaint, and O. Roche, Laboratory landquakes: Insights from experiments into the high-frequency seismic signal generated by geophysical granular flows, Journal of Geophysical Research: Earth Surface **126**, e2021JF006172 (2021).

[44] O. Roche, S. van den Wildenberg, A. Valance, R. Delannay, A. Mangeney, L. Corna, and T. Latchimy, Experimental assessment of the effective friction at the base of granular chute flows on a smooth incline, Physical Review E **103**, 042905 (2021).

[45] P. Favreau, A. Mangeney, A. Lucas, G. Crosta, and F. Bouchut, Numerical modeling of landquakes: Landslides and seismic waves, Geophysical Research Letters **37**, L15305 (2010).

[46] L. Moretti, A. Mangeney, Y. Capdeville, E. Stutzmann, C. Huggel, D. Schneider, and F. Bouchut, Numerical modeling of the Mount Steller landslide flow history and of the generated long period seismic waves, Geophysical Research Letters **39**, L16402 (2012).

[47] M. Yamada, A. Mangeney, Y. Matsushi, and L. Moretti, Estimation of dynamic friction of the akatani landslide from seismic waveform inversion and numerical simulation, Geophysical Journal International **206**, 1479 (2016).

[48] L. Moretti, A. Mangeney, F. Walter, Y. Capdeville, T. Bodin, E. Stutzmann, and A. Le Friant, Constraining landslide characteristics with Bayesian inversion of field and seismic data, Geophysical Journal International **221**, 1341 (2020).

[49] Y. Yan, Y. Cui, J. Guo, S. Hu, Z. Wang, and S. Yin, Landslide reconstruction using seismic signal characteristics and numerical simulations: Case study of the 2017 "6.24" Xinmo landslide, Engineering Geology **270**, 105582 (2020).

[50] H. An, C. Ouyang, and S. Zhou, Dynamic process analysis of the Baige landslide by the combination of DEM and long-period seismic waves, Landslides **18**, 1625 (2021).

[51] H. A. Martin, A. Mangeney, A. Lefebvre-Lepot, B. Maury, and Y. Maday, An Optimization-Based Discrete Element Model for Dry Granular Flows: Application to Granular Collapse on Erodible Beds, https://hal.archives-ouvertes.fr/hal-03790427 (2022), hal-03790427.

[52] S. Popinet, The basilisk code (2013).

[53] F. Bouchut, A. Mangeney-Castelnau, B. Perthame, and J.-P. Vilotte, A new model of Saint Venant and Savage–Hutter type for gravity driven shallow water flows, Comptes Rendus Mathematique **336**, 531 (2003).

[54] F. Bouchut and M. Westdickenberg, Gravity driven shallow water models for arbitrary topography, Communications in Mathematical Sciences **2**, 359 (2004).

[55] A. Mangeney-Castelnau, F. Bouchut, J. Vilotte, E. Lajeunesse, A. Aubertin, and M. Pirulli, On the use of saint venant equations to simulate the spreading of a granular mass, Journal of Geophysical Research: Solid Earth **110**, B09103 (2005).

[56] M. Peruzzetto, A. Mangeney, F. Bouchut, G. Grandjean, C. Levy, Y. Thiery, and A. Lucas, Topography curvature effects in thin-layer models for gravity-driven flows without bed erosion, Journal of Geophysical Research: Earth Surface **126**, e2020JF005657 (2021).

[57] J. J. Moreau, *Nonsmooth mechanics and Applications* (Springer, 1988) pp. 1–82.

[58] M. Jean and J. J. Moreau, Unilaterality and dry friction in the dynamics of rigid body collections, in *1st Contact Mechanics International Symposium* (1992) pp. 31–48.

[59] J. J. Moreau, Numerical aspects of the sweeping process, Computer methods in applied mechanics and engineering **177**, 329 (1999).

[60] M. Jean, The non-smooth contact dynamics method, Computer methods in applied mechanics and engineering **177**, 235 (1999).

[61] J. J. Moreau, An introduction to unilateral dynamics, Lecture Notes in Applied and Computational Mechanics **14**, 1 (2004).

[62] L. Staron and E. J. Hinch, Study of the collapse of granular columns using two-dimensional discrete-grain simulation, Journal of Fluid Mechanics **545**, 1 (2005).

[63] M. Anitescu, Optimization-based simulation of nonsmooth rigid multibody dynamics, Mathematical Programming **105**, 113 (2006).

[64] A. Tasora, D. Negrut, and M. Anitescu, Large-scale parallel multi-body dynamics with frictional contact on the graphical processing unit, Proceedings of the Institution of Mechanical Engineers, Part K: Journal of Multi-body Dynamics **222**, 315 (2008).

[65] F. Radjai and V. Richefeu, Contact dynamics as a nonsmooth discrete element method, Mechanics of Materials **41**, 715 (2009).

[66] V. Acary, F. Cadoux, C. Lemaréchal, and J. Malick, A formulation of the linear discrete Coulomb friction problem via convex optimization, ZAMM Zeitschrift fur Angewandte Mathematik und Mechanik **91**, 155 (2011).

[67] A. Seguin, A. Lefebvre-Lepot, S. Faure, and P. Gondret, Clustering and flow around a sphere moving into a grain cloud, The European Physical Journal E **39**, 63 (2016).

[68] J. Léopoldès, X. Jia, A. Tourin, and A. Mangeney, Triggering granular avalanches with ultrasound, PHYSICAL REVIEW E **102**, 1 (2020).

[69] The Engineering Toolbox, https://www.engineeringtoolbox.com/friction-coefficients-d_778.html (2022), accessed: 2021-12-10.

[70] H. Tang, R. Song, Y. Dong, and X. Song, Measurement of restitution and friction coefficients for granular particles and discrete element simulation for the tests of glass beads, Materials **12**, 10.3390/ma12193170 (2019).

[71] A. Abramian, L. Staron, and P.-Y. Lagrée, The slumping of a cohesive granular column: Continuum and discrete modeling, Journal of Rheology **64**, 1227 (2020).

[72] GDR MiDi, On dense granular flows, The European Physical Journal E **14**, 341 (2004).

[73] P. Jop, Y. Forterre, and O. Pouliquen, A constitutive law for dense granular flows, Nature **441**, 727 (2006).

[74] T. Barker, D. G. Schaeffer, P. Bohorquez, and J. M. N. T. Gray, Well-posed and ill-posed behaviour of the -rheology for granular flow, Journal of Fluid Mechanics **779**, 794 (2015).

[75] E. D. Fernández-Nieto, J. Garres-Díaz, A. Mangeney, and G. Narbona-Reina, 2d granular flows with the μ (i) rheology and side walls friction: a well-balanced multilayer discretization, Journal of Computational Physics **356**, 192 (2018).

[76] M. Yamada, A. Mangeney, Y. Matsushi, and T. Matsuzawa, Estimation of dynamic friction and movement history of large landslides, Landslides **15**, 1963 (2018).

[77] M. Peruzzetto, J.-C. Komorowski, A. L. Friant, M. Rosas-Carbajal, A. Mangeney, and Y. Legendre, Modeling of partial dome collapse of La Soufrière of Guadeloupe volcano: Implications for hazard assessment and monitoring, Scientific Reports **9**, 1 (2019).

[78] A. Guimpier, S. J. Conway, A. Mangeney, A. Lucas, N. Mangold, M. Peruzzetto, M. Pajola, A. Lucchetti, G. Munaretto, T. Sæmundsson, A. Johnsson, L. Le Deit, P. Grindrod, J. Davis, N. Thomas, and G. Cremonese, Dynamics of recent landslides (<20 My) on Mars: Insights from high-resolution topography on Earth and Mars and numerical modelling, Planetary and Space Science **206**, 105303 (2021).

[79] A. Mangeney, P. Heinrich, and R. Roche, Analytical Solution for Testing Debris Avalanche Numerical Models, Pure and Applied Geophysics **157**, 1081 (2000).

[80] G. Faccanoni and A. Mangeney, Exact solution for granular flows, Int. J. Num. Anal. Meth. Geomech. **37**, 1408 (2013).

[81] A. Lucas, A. Mangeney, F. Bouchut, M.-O. Bristeau, and D. Mège, Benchmarking Exercises for Granual Flows, in *The 2007 International Forum on Landslide Disaster Management* (Ho & Li, Hong Kong, 2007).

[82] V. Gueugneau, K. Kelfoun, S. Charbonnier, A. Germa, and G. Carazzo, Dynamics and Impacts of the May 8th, 1902 Pyroclastic Current at Mount Pelée (Martinique): New Insights From Numerical Modeling, Frontiers in Earth Science **8**, 279 (2020).

[83] J. L. Baker, T. Barker, and J. M. N. T. Gray, A two-dimensional depth-averaged mu(I)-rheology for dense granular avalanches, Journal of Fluid Mechanics **787**, 367 (2016).

[84] J. M. N. T. Gray and A. N. Edwards, A depth-averaged mu(I)-rheology for shallow granular free-surface flows, Journal of Fluid Mechanics **755**, 503 (2014).

[85] J. Garres-Díaz, E. D. Fernández-Nieto, A. Mangeney, and T. M. de Luna, A weakly non-hydrostatic shallow model for dry granular flows, Journal of Scientific Computing **86**, 1 (2021).

[86] A. Mangeney-Castelnau, F. Bouchut, J. P. Vilotte, E. Lajeunesse, A. Aubertin, and M. Pirulli, On the use of Saint Venant equations to simulate the spreading of a granular mass: Numerical simulation of granular spreading, Journal of Geophysical Research: Solid Earth **110**, B09103 (2005).

[87] L. Vanel, D. Howell, D. Clark, R. P. Behringer, and E. Clément, Memories in sand: Experimental tests of construction history on stress distributions under sandpiles, Physical Review E - Statistical Physics, Plasmas, Fluids, and Related Interdisciplinary Topics **60**, 5040 (1999).

[88] M. Sperl, Experiments on corn pressure in silo cells–translation and comment of janssen's paper from 1895, Granular Matter **8**, 59 (2006).

[89] B. P. Tighe and M. Sperl, Pressure and motion of dry sand: translation of hagen's paper from 1852, Granular Matter **9**, 141 (2007).

[90] L. Lacaze and R. R. Kerswell, Axisymmetric granular collapse: A transient 3D flow test of viscoplasticity, Physical Review Letters **102**, 3 (2009).

[91] T. Borykov, D. Mège, A. Mangeney, P. Richard, J. Gurgurewicz, and A. Lucas, Empirical investigation of friction weakening of terrestrial and Martian landslides using discrete element models, Landslides 10.1007/s10346-019-01140-8 (2019).

[92] L. Moretti, K. Allstadt, A. Mangeney, Y. Capdeville, E. Stutzmann, and F. Bouchut, Numerical modeling of the Mount Meager landslide constrained by its force history derived from seismic data, Journal of Geophysical Research: Solid Earth **120**, 2579 (2015).

[93] M. Peruzzetto, *Numerical Modeling of Dry and Water-Laden Gravitational Flows for Quantitative Hazard Assessment*, Ph.D. thesis, Université de Paris (2021).

[94] S. Seabold and J. Perktold, Statsmodels: Econometric and statistical modeling with python, in *Proceedings of the 9th Python in Science Conference* (2010).